



HAL
open science

New Constraints on the Origin of the EM-1 Component Revealed by the Measurement of the La-Ce Isotope Systematics in Gough Island Lavas

M. Boyet, R. Doucelance, C. Israel, P. Bonnand, Delphine Auclair, K. Suchorski, Chantal Bosq

► **To cite this version:**

M. Boyet, R. Doucelance, C. Israel, P. Bonnand, Delphine Auclair, et al.. New Constraints on the Origin of the EM-1 Component Revealed by the Measurement of the La-Ce Isotope Systematics in Gough Island Lavas. *Geochemistry, Geophysics, Geosystems*, 2019, 10.1029/2019GC008228 . hal-02156044

HAL Id: hal-02156044

<https://uca.hal.science/hal-02156044>

Submitted on 23 Oct 2019

HAL is a multi-disciplinary open access archive for the deposit and dissemination of scientific research documents, whether they are published or not. The documents may come from teaching and research institutions in France or abroad, or from public or private research centers.

L'archive ouverte pluridisciplinaire **HAL**, est destinée au dépôt et à la diffusion de documents scientifiques de niveau recherche, publiés ou non, émanant des établissements d'enseignement et de recherche français ou étrangers, des laboratoires publics ou privés.

1 **New constraints on the origin of the EM-1 component revealed by the measurement**
2 **of the La-Ce isotope systematics in Gough Island lavas**

3

4 **M. Boyet¹, R. Doucelance¹, C. Israel¹, P. Bonnand¹, D. Auclair¹, K., Suchorski¹, and C.**
5 **Bosq¹**

6

7 ¹Laboratoire Magmas et Volcans, Université Clermont Auvergne, CNRS UMR 6524, OPGC-
8 IRD, F-63000 Clermont-Ferrand, France.

9 Corresponding author: maud boyet (maud.boyet@uca.fr)

10

11

12 **Key Points:**

- 13 • Ce isotopes suggest that the enriched mantle EM-1 sampled by the Gough Island lavas
14 did not incorporate old subducted pelagic sediments.
- 15 • Ce-Nd-Hf isotopes are more consistent with the contribution of subcontinental
16 lithospheric material in the genesis of the EM-1 component.
- 17 • Low Ce/Ce* values measured in Gough Island lavas are not explained by the
18 incorporation of pelagic sediments in the mantle source.

19 **Abstract**

20 Hotspot lavas show a large diversity of isotope compositions resulting from the recycling of
21 surface material into the convective mantle. Amongst the mantle end-members, EM-1 (enriched
22 mantle) is widely debated and scenarios involving either old pelagic sediments subducted into
23 the deep mantle or subcontinental lithospheric material incorporated at shallow depths are
24 commonly evoked. We selected 12 lavas from Gough Island (South Atlantic Ocean) for the
25 measurement of ^{138}La - ^{138}Ce , ^{147}Sm - ^{143}Nd and ^{176}Lu - ^{177}Hf isotope systems. Results show limited
26 ranges for $\epsilon^{143}\text{Nd}$, $\epsilon^{138}\text{Ce}$ and $\epsilon^{176}\text{Hf}$ values, and Ce/Ce^* do not correlate with measured isotope
27 ratios. Cerium isotope compositions allow us to exclude the contribution of old sedimentary
28 material carrying a negative, elemental cerium anomaly in the mantle source. Pelagic sediments
29 are indeed characterized by strongly negative, elemental cerium anomalies and also high La/Ce
30 ratios. Modelling a primitive mantle source contaminated by 0.4 to 2.2% of different 2.5 Ga-old
31 pelagic components is able to reproduce the lowest Ce/Ce^* values. However, the cerium isotope
32 measurements show $\epsilon^{138}\text{Ce}$ values between -0.39 and 0.15, too low to give support to the
33 incorporation of recycled pelagic sediments in the mantle source of the lavas. Our results suggest
34 that the incorporation of subcontinental lithospheric material at shallow depths during the plume
35 ascent is a more suitable model to explain the formation of the EM-1 component. Hafnium and
36 Nd isotopes also support this scenario. Subcontinental lithosphere sampled via kimberlites and
37 lamproites has isotopic compositions that plot generally below the mantle array, a signature that
38 is also seen in Gough lavas.

39

40 **1 Introduction**

41 Plate tectonics leads to the recycling of material from the surface to the Earth's interior via
42 subduction. The penetration of cold slabs into the deep mantle has been observed via seismic
43 tomography [*Grand et al., 1997; van der Hilst et al., 1997*] and can also be tracked using
44 different geochemical proxies. For example, hafnium isotope compositions measured in lavas
45 from several Hawaiian volcanoes have revealed the participation of old pelagic sediments in
46 their deep source [*Blichert-Toft et al., 1999*]. Similarly, mass independent $\Delta^{33}\text{S}$ measured in
47 olivine-hosted sulphides from Mangaia and Pitcairn lavas are explained by the recycling of
48 surface material that existed before the Great Oxygenation Event (GOE) in a reduced atmosphere
49 [*Cabral et al., 2013; Delavault et al., 2016*]. In a more general way, extreme Pb-Sr-Nd isotope
50 signatures identified in Ocean Island Basalts (OIB) and defining the mantle end-members
51 (HIMU, EM-1, EM-2: *Zindler and Hart [1986]*) have been interpreted as proof of deep recycling
52 of surface components [*Hofmann and White, 1982; White and Hoffmann, 1982*]. Geochemical
53 modelling involves generally recycling of old reservoirs (2 Ga) suggesting that very old
54 materials can be preserved in the convective mantle, in agreement with dynamical model results
55 [e.g. *Chauvel et al., 1992; Tackley, 2015*].

56 The exact nature of the different mantle components is widely discussed in the literature
57 published over the last 30 years and some debates are still ongoing [*Jackson et al., 2018*]. Here
58 we will focus on the enriched mantle called EM-1 that has been clearly identified in lavas from
59 Gough Island, South Atlantic Ocean. Two enriched mantle components have been defined (EM-
60 1 and EM-2). They have similar unradiogenic Nd isotope ratios but are different for Sr and Pb
61 isotopes [*Zindler and Hart, 1986*]. Two different origins for the EM-1 component are proposed,
62 either 1) the involvement of subducted pelagic sediments [e.g. *Chauvel et al., 1992; Eisele et al.,*

63 2002], or 2) the incorporation of continental material (sub-lithospheric mantle and/or lower
64 crust) at shallow depths [*Hawkesworth et al.*, 1986; *Carlson et al.*, 1996; *Escrig et al.*, 2005;
65 *Class and le Roex*, 2006].

66 Previous proportion estimates made on the basis of Sr-Nd-Pb isotopes for a pelagic component in
67 the lava sources of samples from South Atlantic Ocean islands (e.g. Gough and Tristan da
68 Cunha) are up to 3 % [*le Roex et al.*, 1990; *Weaver et al.*, 1986]. This agrees with the more
69 recent value of 2 % that was proposed from the measurement of the $\delta^{18}\text{O}$ in the major
70 phenocrysts present in Gough lavas [*Harris et al.*, 2000], and also with elemental cerium
71 anomalies recorded in Gough Island that were attributed to the participation of 0.5 % of a
72 recycled sediment component [*Class and le Roex*, 2008]. Depletion in cerium relative to its two
73 neighbors (La, Pr) is quantified with the Ce/Ce* notation ($\text{Ce/Ce}^* = (\text{Ce}_N / (\text{La}_N^{0.5} \times \text{Pr}_N^{0.5}))$)
74 where Ce_N , La_N and Pr_N are Ce, La and Pr concentrations normalized to chondrite or PAAS
75 values). It is commonly observed in pelagic sediments and it reflects the particular behavior of
76 cerium that exists under two valence states (3+ and 4+). Furthermore, it has recently been shown
77 that only very small, elemental cerium anomalies could be generated in volcanic samples during
78 magmatic processes such as batch melting and/or fractional crystallization [*Bellot et al.*, 2018]).
79 The aim of the present study is to combine the measurement of Rare Earth Elements (REE) and
80 of several isotope systems (^{147}Sm - ^{143}Nd , ^{176}Lu - ^{176}Hf , ^{138}La - ^{138}Ce) in a series of well-
81 characterized Gough Island lavas in order to better constrain the EM-1 end-member. The use of
82 the ^{138}La - ^{138}Ce isotope systematics ($T_{1/2} = 292.5 \text{ Ga}$; *Tanimizu* [2000]) is particularly well-
83 adapted since marine sediments formed in equilibrium with seawater are characterized by
84 negative, elemental cerium anomaly. Calculations show that significant variations of their

85 $^{138}\text{Ce}/^{142}\text{Ce}$ ratio can be generated in less than 100 Ma (see Figure 1 in *Bellot et al.* [2015]).
86 Furthermore, due to their particular REE patterns, marine sediments acquire by radiogenic
87 ingrowth Ce-Nd isotopic signatures that strongly deviate from those of other mantle reservoirs.
88 Thus, on a timescale of 2 Ga, even a small contribution of 1 % of a sedimentary component
89 carrier of a negative, elemental cerium anomaly is likely to be identified by measuring
90 $^{138}\text{Ce}/^{142}\text{Ce}$ ratios. Calculated increases with such proportions that will be presented in detail in
91 the discussion range from 0.5 to 12 ϵ -units depending of the composition of the sedimentary
92 component (La/Ce ratio and REE concentrations), the mixing considered and how it melts. If a
93 pelagic component is indeed present in the source of Gough lavas, combining Ce isotope
94 measurements with $^{176}\text{Hf}/^{177}\text{Hf}$ and $^{143}\text{Nd}/^{144}\text{Nd}$ ratios will allow us to specify its proportions. On
95 the other hand, the absence of coupled variations between the $^{138}\text{Ce}/^{142}\text{Ce}$ ratio and the elemental
96 cerium anomaly in Gough samples will favor other scenarios, in particular those involving the
97 incorporation of subcontinental lithospheric mantle into the mantle melt source [*Konter and*
98 *Becker, 2012*].

99

100 **2 Geological setting and sample selection**

101 Gough Island is a very small island of 65 km² located in the south part of the Atlantic Ocean
102 (400 km to the southeast of Tristan da Cunha Island), firstly studied by *Le Maitre* [1962]. The
103 magmatic activity lasted about 1 Ma from the emplacement of the Lower Basalts to that of the
104 youngest Upper Basalts at 0.13 Ma [*le Roex, 1985*]. Lavas range from picrite basalts to trachytes.
105 The petrology and geochemistry of the 12 samples analyzed in the present study were previously
106 described by *le Roex* [1985] and *Class and le Roex* [2008]; they were selected to cover the entire

107 range of Ce anomalies measured in a superset of 38 samples. On average the elemental cerium
108 anomaly measured in the 12 lavas is 0.98 and it varies from 0.94 to 1.04. Sample locations are
109 reported on the geological map presented as Figure 1 in *Class and le Roex* [2008].

110

111 **3 Analytical methods**

112 3.1 Major and Rare Earth Elements

113 Major-element concentrations were determined in the Laboratoire Magmas et Volcans (LMV) by
114 ICP-AES (Jobin-Yvon ULTIMA C) after sample dissolution by lithium-metaborate flux-fusion.
115 The quoted precision is calculated from the repeated measurement of the certified USGS
116 reference material BHVO-2 analyzed in the same conditions than Gough lavas.

117 For trace-element measurements 50 to 100 mg of samples were dissolved using a 3:1 mixture of
118 HF and HNO₃ concentrated acids maintained during 48 hours on a hotplate at 75 °C. Once dried,
119 samples were dissolved in 7 M HNO₃ and dried again, then 6 M HCl was added and beakers
120 were placed at 90 °C for 24 hours. Once the solutions were perfectly clear, samples were split
121 into two fractions: ~10 % for the measurement of REE contents (results noted LMV1 in the
122 manuscript); and ~90 % to determine Ce-Nd-Hf isotopic compositions. All samples were also
123 dissolved a second time using the same protocol, but for REE content measurements only (no
124 aliquot, results noted LMV2 in the manuscript). Different techniques of sample preparation
125 including dissolution and dilution were tested on the BHVO-2 reference material in order to
126 define more precisely the reproducibility and precision on the elemental cerium anomaly (see
127 section 4.1). All measurements were performed using the LMV Agilent-ICP-MS in Clermont-

128 Ferrand. Counts per second were calibrated using a synthetic solution (CMS) containing ~60
129 trace elements at 1 ppb (LMV1) or the certified rock standard BHVO-2 (LMV2). The blank and
130 reference materials were measured every four samples. Certified rock standards BIR-1 and/or
131 BEN were also analyzed in order to test the whole protocol (See supplementary Table 1). The
132 method used here allows to correct for oxide interferences and for the instrumental drift if
133 significant and to subtract the blank. Samples were measured in 0.5 M-HNO₃ – 0.05 M-HF with
134 a dilution factor of about 3500.

135

136 3.2 Ce-Nd-Hf isotopes

137 Once dissolved, the samples were loaded on a cation resin (AG-W50 X8, 200-400 mesh, ~5ml)
138 in a 1 M-HCl – 0.1 M-HF mixture. The Hf fraction was directly collected whereas the REE
139 fraction was purified from the major elements in 2.5 M-HCl and collected in 4 M-HCl. The Hf
140 fraction was purified during a second step using 1 ml of LN-spec resin (100-150 µm) with
141 different acids (HCl, citric acid-HNO₃-HF) and collected using a 6 M-HCl – 0.4 M-HF solution.
142 Details of the whole procedure are reported in *Carlson et al.* [2006]. The Nd and Ce fractions
143 were separated by oxidizing the cerium in Ce⁴⁺ (using the protocol inspired by *Tazoe et al.*
144 [2007] and modified by *Bonnand et al.* [2019]). Lastly Nd was separated from Sm that creates
145 isobaric interferences on mass 144 on a LN spec column using 0.2 M-HCl [*Rizo et al.*, 2011].

146 Hafnium isotopes were measured on the LMV, Neptune Plus, Multi-Collector Inductively-
147 Coupled-Plasma Mass Spectrometer (MC-ICPMS) coupled to an Aridus II desolvating nebulizer
148 system at solution concentrations ranging from 20 to 50 ppb. Instrumental mass bias effects were
149 corrected for using an exponential law and $^{179}\text{Hf}/^{177}\text{Hf} = 0.7325$. In order to monitor the

150 instrument performance, two synthetic solutions (JMC 475 at 20 ppb and Alfa Aesar at 30 ppb)
151 were run every three samples. $^{176}\text{Hf}/^{177}\text{Hf}$ for JMC and Alfa Aesar are 0.282155 ± 0.000009 and
152 0.282189 ± 0.000006 , respectively (2SD, $n = 16$). The two rocks standards BHVO-2 (two
153 dissolutions) and BCR-2 were also measured using the same analytical protocol than Gough
154 samples. Measured $^{176}\text{Hf}/^{177}\text{Hf}$ ratios for BHVO-2 (0.283092 ± 0.000003 and $0.283094 \pm$
155 0.000003) and BCR-2 (0.282861 ± 0.000004) are in good agreement with published results (see
156 *Chauvel et al.* [2011] and the GeoREM compilation).

157 Neodymium isotopes were measured using the LMV, Triton PlusTM, Thermal Ionization Mass
158 Spectrometer (TIMS) in static mode. Isotope ratios were corrected for mass fractionation using
159 an exponential law and $^{146}\text{Nd}/^{144}\text{Nd} = 0.7219$. The Nd standard JNdi-1 was measured 10 times
160 during the entire analytical session (mass spectrometer used only for the Nd measurement of
161 these samples during this period) and the average $^{143}\text{Nd}/^{144}\text{Nd}$ ratio is 0.512101 ± 0.000004
162 (2SD) in agreement with dynamic measurements [*Garçon et al.*, 2018].

163 Cerium isotopes were also measured using the LMV, Triton PlusTM TIMS. The whole analytical
164 procedure is detailed in *Bonnand et al.* [2019]. The contribution from the ^{140}Ce peak (tailing
165 effect) was subtracted to intensities measured at masses 136 and 138 ($\Delta^{138}\text{Ce}$, the difference
166 between tailing-corrected and tailing-uncorrected data is 0.85 epsilon-unit) and Ce isotope ratios
167 were mass-fractionation-corrected using an exponential law and $^{136}\text{Ce}/^{142}\text{Ce} = 0.01688$.
168 Measurements of Ce reference materials Ce_{LMV} and Ce_{AMES} gave $^{138}\text{Ce}/^{142}\text{Ce}$
169 $= 0.02257053 \pm 0.00000061$ (2SD, $n=48$) and $^{138}\text{Ce}/^{142}\text{Ce} = 0.02257426 \pm 0.00000068$ (2SD,
170 $n=25$), respectively [*Bonnand et al.*, 2019]. $^{138}\text{Ce}/^{142}\text{Ce}$ ratios measured for the two USGS rock
171 standards BCR-2 and BHVO-2 are $0.02256689 \pm 0.00000055$ (2SD, $n = 5$) and $^{138}\text{Ce}/^{142}\text{Ce} =$

172 0.02256489 ± 0.00000047 (2SD, n = 2), respectively. These values agree with previous
173 measurements [Doucelance *et al.*, 2014; Bellot *et al.*, 2015; Willig and Stracke, 2018].

174

175 **4 Results**

176 4.1 Determination of the elemental cerium anomaly

177 The range of Ce/Ce* determined for Gough Island lavas is relatively small and the variation does
178 not exceed 10 % when considering our data and previous results of *Class and le Roex* [2008]. To
179 ensure a robust interpretation of the data two parameters must be verified: 1) the analytical
180 precision obtained by ICP-MS; and 2) the chemical treatment/protocol used for the sample
181 dissolution and for the solution preparation before ICP-MS analysis. Trace element and isotope
182 measurements are generally combined with trace elements being determined from a small aliquot
183 of the sample after the first dissolution. Thus, in order to address the potential problem of adding
184 too small volumes of acid to obtain a perfect dissolution of all elements, we have tested different
185 protocols using the BHVO-2 rock standard. The first dissolution is identical for all the tests; it
186 uses about 50 mg of BHVO-2 and a 3:1 mixture of concentrated HF and HNO₃ acids placed in
187 Savillex vials on a hotplate at 75 °C for 48 hours. Experiments labelled A to E were treated with
188 HClO₄ to expel fluorides and volumes of 7 M-HNO₃ varying from 5 to 30 ml were considered to
189 get all of the samples back in solution, whereas experiments labelled F to K excluded HClO₄ and
190 used a constant volume of 20 ml with either 7 M-HNO₃ or 6 M-HCl (Table 1). For trace element
191 measurements, nitric acid is currently used to make the concentrated stock solution.
192 Hydrochloric acid, however, is favored when trace elements and isotopes are measured on the
193 same dissolution. The A to K beakers were then placed on a hot plate for 24 hours and an aliquot

194 was taken up and dried before MC-ICP analysis in 0.5 M-HNO₃ – 0.05 M-HF solutions with a
195 dilution factor of 3500. Measurements were performed using the LMV, Agilent 7500,
196 quadrupole ICP-MS. Each solution was measured twice and concentrations were calibrated using
197 repeated measurements of solutions containing 62 trace elements diluted to concentrations of 1
198 and 10 ppb. These solutions were also used to monitor and correct for the instrumental drift over
199 the analytical sequence. Six blanks were prepared following the same protocols and subtracted to
200 the measurements. Results are presented in Table 1 and expressed in $\Delta\text{Ce}/\text{Ce}^*$ (%) that
201 corresponds to the variation of the measured, elemental cerium anomaly of BHVO-2 relative to
202 its theoretical value (1.006 given in GeoREM). The 11 experiments give similar results with a
203 total variation lower than 1 %. We conclude that the type of acid used and the final volume for
204 the concentrated solution have no influence on the measurement of the elemental cerium
205 anomaly. We did not identify any interference on LREE coming from Ca perchlorates either
206 [*Longerich, 1993*].

207

208 4.2 Major and Rare Earth Element contents of Gough samples

209 Gough Island lavas have basaltic compositions with SiO₂ and MgO contents ranging from 47.4
210 to 51.1 wt.% and from 3.1 to 14.0 wt.%, respectively. Rocks have been classified using the Total
211 Akali (Na₂O+K₂O) Silica (TAS) diagram. They are all basalts or trachy-basalts except sample
212 ALR34G that is in the basaltic trachy-andesite field. All samples but one (ALR45G) have LOI <
213 0.7 wt.% (Table 2). Our new measurements are in good agreement with analyses previously
214 published [e.g. *le Roex, 1985*].

215 Rare earth elements have been measured with the aim of determining the cerium anomalies in
216 these samples (Ce/Ce^*). The anomalies are relatively small (down to 0.92, see Table 2) and
217 measurements are challenging. Calculations were made using $Ce/Ce^* = (Ce_N / (La_N^{0.5} \times Pr_N^{0.5}))$
218 with a normalization to CI chondrites from *Pourmand et al.* [2012]. Using these values,
219 calculated Ce/Ce^* generally increase by 0.01 relative to a chondritic normalization to
220 *McDonough and Sun* [1995]. Considering data on the CI chondrite Orgueil published by *Barrat*
221 *et al.* [2012] gives identical results. Ce/Ce^* measured in the two standards BEN and BIR-1 are in
222 perfect agreement with literature values with $Ce/Ce^* = 0.984 \pm 0.022$ and $Ce/Ce^* = 0.967 \pm$
223 0.032 , respectively (the uncertainty here corresponds to the standard deviation calculated from
224 four repeated measurements). For example, the compilation of BIR-1 measurements gives
225 Ce/Ce^* between 0.93 and 0.99 (average value of 0.96 ± 0.04 , 2SD, $n = 11$, *Pourmand et al.*
226 [2012]).

227 Gough samples were measured twice and results are presented in Table 2. The difference
228 between the two calibrations (LMV1 and LMV2) is lower than 2 % except for three samples
229 (ALR34G, ALR40G, ALR41G) for which it is up to 4.5 %. The elemental cerium anomaly
230 ranges from 0.93 to 1.05: on average it is equal to 0.98 ± 0.06 (2SD) in method 1 and to $0.99 \pm$
231 0.06 (2SD) in method 2. Our results show a greater dispersion than those obtained by *Class and*
232 *le Roex* [2008] with differences up to 8 % (sample ALR41G). Low Ce/Ce^* are systematically
233 determined for samples ALR46G, ALR52G and ALR64G (Figure 1). For instance, ALR52G was
234 measured four times by *Class and le Roex* [2008] and all the determinations gave an elemental
235 cerium anomaly of 0.92 that agrees with our value of 0.93 (two duplicates). Although the
236 dispersion of the data is clearly more important than that observed on BHVO-2 tests, only a few
237 samples appear to have resolved negative cerium anomalies ($Ce/Ce^* < 1$). Results obtained by

238 *Willbold and Stracke* [2006] on a different series of samples coming from Gough Island are also
239 reported on Figure 1; they are all in agreement with ours except one sample (not shown on the
240 figure) that has a Ce/Ce* of 0.84. This sample shows a deficiency of incompatible, fluid-mobile
241 trace elements relative to similarly incompatible, fluid-immobile ones, strongly suggesting that
242 its depletion in cerium is related to alteration processes. Using our dataset, no correlation is
243 identified between the elemental cerium anomaly and geochemical proxies (e.g. U/Th). Rare
244 earth element patterns measured in Gough Island samples are presented in Figure 2. They show
245 the enrichment characteristic of OIB in Light REE compared to Heavy REE.

246

247 4.3 Ce-Nd-Hf isotopes

248 Gough samples show very small variations of the Ce, Nd and Hf isotope ratios with $\epsilon^{143}\text{Nd}$,
249 $\epsilon^{138}\text{Ce}$ and $\epsilon^{176}\text{Hf}$ values between -1.03 and -1.99, -0.39 and 0.15, and -3.1 and -1.5, respectively
250 (Table 3). Few samples were previously measured for Nd isotopes [*Class and le Roex*, 2008] and
251 both sets of results are in good agreement with an average difference of 0.3 epsilon. Ce isotope
252 data presented for two Gough samples in *Willig and Stracke* [2019] are in good agreement with
253 our measurements. Data are presented in binary plots in Figure 3. Gough samples define a
254 positive co-variation in the ϵHf vs. ϵNd plot (Figure 3A). Only sample ALR45G falls slightly
255 outside, having a relatively high $\epsilon^{176}\text{Hf}$ (-1.79) for a low $\epsilon^{143}\text{Nd}$ (-1.99). Conversely, Gough lavas
256 show a slight negative trend in the ϵNd vs. ϵCe plot (Figure 3B). Lastly, there is no well-defined
257 trend in the ϵHf - ϵCe plot (Figure 3C).

258

259 **5 Discussion**

260 5.1 No significant contribution of a recycled, «pelagic» component in the mantle source
261 of Gough lavas

262 The involvement of pelagic sediments in the mantle source of EM-1-like plumes may explain
263 their specific Sr-Nd-Pb isotope signatures [*Chauvel et al.*, 1992]. Isotope modelling shows that
264 such a component must have been recycled into the mantle via subduction a long time ago and
265 recycling ages between 1.5 and 2.0 Ga are commonly evoked. The discovery of mass
266 independent $\Delta^{33}\text{S}$ in samples from Mangaia and Pitcairn lavas (Pacific Ocean) increases the time
267 scale of recycling since $\Delta^{33}\text{S}$ signatures must have been acquired before the Great Oxygenation
268 Event (GOE) by photochemical reactions in anoxic atmosphere [*Cabral et al.*, 2013; *Delavault et*
269 *al.*, 2016]. These two hotspots are of HIMU and EM-1 types and they have been suggested to
270 incorporate surface material recycling [*Weaver*, 1991; *Chauvel et al.*, 1992].

271 Negative, elemental Ce anomalies are commonly reported in fore-arc drilled sediments and
272 trenches having the lowest Ce/Ce* are those least fed by detrital sediments from continental
273 erosion [*Plank*, 2013]. In oxidizing conditions cerium exists under the 4+ valence state whereas
274 neighboring REE remain in the 3+ form. Thus, the negative Ce anomaly of seawater (Ce/Ce*<1)
275 reflects the strongly insoluble character of Ce(IV), whereas Fe-Mn crusts and MnO clays
276 preferentially scavenge Ce(IV) and thus have positive Ce anomalies (Ce/Ce*>1) [*Elderfield and*
277 *Greaves*, 1982]. The cerium isotopic compositions of Gough samples do not show any
278 correlation with the elemental cerium anomaly (Figure 4). If the mantle source of the lavas was
279 carrying a negative cerium anomaly and had a high La/Ce ratio, it should have developed with
280 time a radiogenic $^{138}\text{Ce}/^{142}\text{Ce}$ signature, as illustrated by *Bellot et al.* [2015] for short time

281 duration in comparison to 1.5 and 2.5 Ga usually assumed for recycling in OIB mantle sources.
282 We have modelled the radioactive ingrowth of ^{138}Ce of three distinct, marine-sediment reservoirs
283 having fractionated La/Ce ratios and different REE patterns (Table 4): 1) the first reservoir has
284 the mean composition of carbonate sediments recovered at DSDP Site 495 on the subducting
285 Cocos Plate in the middle American trench [*Patino et al.*, 2000]; 2) the second one is similar to
286 the Pacific Authigenic Weighted Mean sediments (PAWS) [*Hole et al.*, 1984] that was defined
287 from a sequence of pelagic oozes sampled on the Nasca Plate (Leg 34); and 3) the last one
288 averages the compositions of sediments drilled in five different trenches located far from
289 continents (Kemadec, Tonga, Vanuatu, Marianas and Izu-Bonin) and thus protected from detrital
290 inputs [*Plank*, 2013]. The three reservoirs, namely R1, R2 and R3, are characterized by low
291 Ce/Ce* of 0.13, 0.18 and 0.73, respectively. With time they acquire strongly radiogenic ^{138}Ce
292 isotope compositions with deviations in epsilon as high as 140, 100 and 17 for a decay time of
293 2.5 Ga. The elemental cerium anomaly in the reservoir R3 is similar to that determined for
294 biosiliceous sediments from the Mariana trench (DSP site 801) by *Bellot et al.* [2018]. Ce/Ce*
295 ratios calculated for Gough Island lavas were plotted against their Sr isotope compositions by
296 *Stracke* [2012]. No correlation is observed and adding our samples does not modify the previous
297 observation (Sr isotope compositions from *Class and Le Roex* [2008]). Tracking the participation
298 of recycled sediments in the mantle source of Gough lavas with the elemental Ce anomaly is thus
299 challenging and more robust conclusions should be obtained by measuring the Ce isotope
300 composition of the samples.

301 Ce/Ce* together with isotope ratios resulting from the mixing between a deep mantle source of
302 FOZO-type (see Table 4 for trace element and isotope characteristics) and a 2.5 Ga-old
303 subducted component are presented in Figure 5. Only the values corresponding to the range of

304 negative cerium anomalies of Gough lavas (Ce/Ce^* down to 0.92) are reported. In the first model
305 (Fig. 5A) the FOZO source is contaminated by different proportion of sediments having R1, R2
306 or R3 characteristics. The mixture is considered homogeneous and then can be modelled as a
307 solid-solid mixture. In the second model we consider the same mixtures but the approach used by
308 *Class and le Roex* [2008], e.g. $D = 0$ for LREE and sediment melts derived by 25% partial
309 melting of a sediment protolith (Fig. 5B). In the third model the sediments were subducted as a
310 thin layer on top of the oceanic crust (OC) in proportion 5:95. During the melting we assume a
311 productivity 10 times higher for sediments than for the mafic components (OC-FOZO).

312 The two first models lead to the same results, only the proportion of sediment changes. The
313 proportions of the sediment component required to generate an elemental cerium anomaly of
314 0.92 are 1.2 %, 1.6 % and 2.2 % for reservoirs 1, 2 and 3, respectively. In the second case the
315 sedimentary proportion is always lower than 1%, in agreement with estimates proposed by *Class*
316 *and le Roex* [2008]. However, such proportions strongly increase the $\epsilon^{138}Ce$ relative to its initial,
317 FOZO-like composition with maximum values reaching 4 for the most, REE-enriched sediments
318 (reservoir R3). Gough samples have a very narrow range of isotopic composition ($\epsilon^{138}Ce$ varying
319 from -0.39 to 0.15) and, as mentioned in the previous section, no correlation is observed between
320 the elemental cerium anomaly and the cerium isotope composition (Figure 4). In the third model
321 (OC-sediments-FOZO), the calculated isotope compositions are less radiogenic (Fig. 5C). To
322 reach a Ce/Ce^* value of 0.92, the sedimentary proportion is between 1.4 and 4% and the $\epsilon^{138}Ce$
323 increases from 0.5 to 2.8 ϵ -units in function to the composition of the sediments. Mixing lines
324 calculated using the composition of R1 and R2 sedimentary reservoirs pass through the Gough
325 Island samples characterized by the lowest Ce/Ce^* values. However, the models fail to explain
326 all other data. As a consequence, cerium isotopic compositions measured in EM-1-like lavas

327 make it possible to exclude the contribution of material carrying a negative, elemental cerium
328 anomaly in their mantle source, at least if the marine sediments have been subducted a long time
329 ago (> 1.5 Ga). During this time period the radioactive production of ^{138}Ce is large enough to be
330 measured in the third model (+0.5 ϵ -unit for R1 and R2; +1.8 ϵ -unit for R3). As a consequence,
331 the involvement of old pelagic sediments characterized by low Ce/Ce^* values in the EM-1-like
332 OIB sources should result in an offset of their isotopic compositions in the $\epsilon^{143}\text{Nd}$ vs $\epsilon^{138}\text{Ce}$ -
333 diagram with respect to the mantle array. However, the number of data available in the literature
334 is not sufficient to investigate in detail this effect. The mantle array is defined from MORB and
335 OIB data and EM-1 samples strongly constrain the best-fit line because they represent extreme
336 points on the correlation (5 measurements obtained from Gough and Tristan hotspots [*Willig and*
337 *Stracke, 2019*]).

338 Modern sediments are conventionally used in geochemical modelling (as done here) and it is
339 questionable whether they represent good analogues of ancient sediments. Most Precambrian
340 carbonate samples are stromatolites formed at shallow water-depth close to continents. Samples
341 coming from different continents including Australia (3.45 Ga) [*Van Kranendonk et al., 2003*],
342 South Africa (2.52 Ga) [*Kamber and Webb, 2001*] and the Canadian Shield (2.94 and 2.8 Ga)
343 [*Riding et al., 2014; Satkoski et al., 2017*] show fractionated La/Ce ratios due to La enrichment
344 rather than Ce depletion. Ce/Ce^* calculations using the chondrite normalization (rather than
345 PAAS as commonly used in sediment studies) yield values down to 0.73. However, the REE
346 concentrations of all of these rocks are extremely low with a few hundred ppb as maximum
347 values. Thus, if the mantle source of OIB involved this kind of material this would not change
348 the cerium isotopic composition of the lavas nor their Ce/Ce^* , at least if the sedimentary
349 contribution does not exceed a few %. The marine carbonate recycling hypothesis has been

350 investigated in detail by *Castillo* [2015] in order to explain the strongly radiogenic Pb ratios
351 coupled to unradiogenic Sr that are measured in HIMU-like basalts. Questions about the
352 chemical signatures of marine carbonates and the preservation of chemical signatures through
353 time are clearly raised. Marine carbonates are primarily proposed for their high U/Pb ratio, but
354 during Archean times U may not be really abundant in seawater because of the reducing
355 atmosphere. Like for cerium, the GOE probably marks an important transition in the behavior of
356 all redox sensitive elements.

357

358 5.2 Subcontinental lithospheric material in the EM-1 component

359 All the hotspot “classifications” relate the Tristan da Cunha - Gough hotspot to a deep-rooted
360 mantle plume [*Boschi et al.*, 2007; *Courtillot et al.*, 2003; *French and Romanowicz*, 2015].
361 However, it is an exception to most deep hotspots because samples from Tristan da Cunha -
362 Gough samples have low $^3\text{He}/^4\text{He}$ ratios similar to those of the restricted MORB range rather
363 than high values [*Kurz et al.*, 1982]. It is also unusual in its seafloor appearance, showing an
364 increasingly wide track toward present-day Gough and Tristan [*O'Connor and Jokat*, 2015]. The
365 incorporation of continental material has been proposed as origin of the EM-1 mantle
366 component, including the shallow incorporation of subcontinental materials [e.g. *Carlson et al.*,
367 1996; *Class and le Roex* 2006; *Konter and Becker* 2012]. Mixing models developed to reproduce
368 the $^{87}\text{Sr}/^{88}\text{Sr}$, $^{143}\text{Nd}/^{144}\text{Nd}$ and $^{206}\text{Pb}/^{204}\text{Pb}$ ratios of Gough lavas are presented in *Konter and*
369 *Becker* [2012]. The required proportion of subcontinental lithosphere mantle melt or granulite
370 melt to the deep mantle (equivalent to the FOZO component) is high (up to 50 %). The
371 upwelling of deep mantle contaminated with subcontinental material or lower crust provides an

372 EM-1 component located at shallow depth in the mantle, explaining the correlation observed
373 between the EM-1 occurrence and both shear wave speed anomalies at 200 km and plume depth
374 extent [*Konter and Becker, 2012*]. The incorporation of a large quantity of subcontinental
375 material also explains the low $^3\text{He}/^4\text{He}$ ratios measured in the samples.

376 Gough samples have Hf-Nd isotopic compositions that plot slightly below the mantle array
377 (Figure 6A); they are characterized by negative $\Delta\varepsilon_{\text{Hf}}$ values between -2 and -3 (the $\Delta\varepsilon_{\text{Hf}}$
378 notation reflects the distance to the mantle array line, see *Johnson and Beard [1993]*). Samples
379 recording the largest displacements below the mantle Hf-Nd array are lamproites and kimberlites
380 [e.g. *Nowell et al., 2004; Tappe et al., 2013*]. Hf-Nd isotope data for lamproites and Group II
381 kimberlites are plotted on Figure 6B. The samples are from various locations and they show
382 contrasted isotope compositions in the Hf-Nd isotopic space. Ages of lamproites are 0.1-3.1 Ma
383 for Leucite Hills, 4.5-15.6 Ma for Anatolia, 143 Ma for Siberia and 1224 Ma for samples coming
384 from the Dharwar craton. We did not find any data for lamproites from the South African craton
385 in the literature or in the GEOROC database. On the contrary all plotted kimberlites from Group
386 II are from the South African craton. More precisely, occurrences are both on- and off-craton
387 kimberlites from the Archaean Kaapvaal craton and from the Proterozoic Namaqua–Natal belt
388 (see sample description in *Becker and le Roex [2006]*). Two binary mixing models are also
389 plotted on Figure 6B. These models consider a deep mantle source similar in compositions to
390 FOZO interacting with a component coming from the subcontinental lithospheric mantle
391 resembling either to i) the average composition of Swartruggens Group II kimberlites (green
392 curve) or ii) the average composition of Leucite Hills lamproites (blue curve). Using an average
393 value of worldwide samples would not really make sense especially when considering the
394 diversity of isotopic compositions measured for lamproites. Lamproites from Leucite Hills were

395 selected because they are the most recent samples. Although the samples from Swartruggens
396 have the most negative $\Delta\epsilon_{\text{Hf}}$ values amongst kimberlites, the calculated mixing curve passes
397 slightly above the Gough field. Selecting the samples having the most negative $\Delta\epsilon_{\text{Hf}}$ values
398 would, however, explain the isotopic compositions of Gough lavas. In these calculations the
399 isotope compositions of Gough samples are roughly reproduced for proportions of kimberlite-
400 like melts ranging from 10 to 20 % and for proportions of lamproite-like melts ranging from 15
401 to 30 %. These proportions are slightly lower than those estimated by *Konter and Becker* [2012]
402 with contributions from the continental component up to 50%.

403 Contrary to Gough, Tristan da Cunha Island samples plot perfectly on the Mantle array in the
404 $\epsilon_{\text{Hf}}-\epsilon_{\text{Nd}}$ diagram (Figure 6A). Gough and Tristan da Cunha tracks were subdivided in all isotope
405 diagrams by *Rohde et al.* [2013]. The Gough sub-track generally displays more enriched isotopic
406 compositions. Spatial geochemical zonings were previously reported in hotspot tracks in the
407 Pacific Ocean, with Hawaii being the most famous example [e.g. *Abouchami et al.*, 2005;
408 *Farnetani and Hofmann*, 2009; *Weis et al.*, 2011]. The Tristan da Cunha - Gough plume was the
409 first example of a zoned plume located above the margin of the African superplume and it has
410 been proposed that the enriched source of Gough sub-track reflects the African superplume
411 composition whereas samples from the Tristan da Cunha sub-track record a larger contribution
412 of the surrounding depleted mantle [*Rohde et al.*, 2013]. More recently the spatial geochemical
413 zonation has been explained by a plume source migration with time [*Hoernle et al.*, 2015]. The
414 enriched Gough component is present in the earlier (70–132 Ma) history of the hotspot contrary
415 to the less-enriched Tristan. The early hotspot would tap only LLSVP (low shear-wave velocity
416 province) and with time the plume stem migrates towards the LLSVP boundary. Here we favor

417 instead the idea that the Gough Island lavas have incorporated a larger proportion of
418 subcontinental lithospheric material than those from the Tristan da Cunha sub-track. The location
419 of this component is still discussed. The participation of this component on a large spatial scale
420 (Tristan-Gough-Discovery Rise) suggests the recycling of subcontinental lithospheric material
421 through the lower mantle rather than interaction during the rise of the plume [*Schwindrofska et*
422 *al.*, 2016].

423

424 5.3 Origin of the elemental cerium anomalies

425 The low Ce/Ce* values determined for a few lavas from Gough Island cannot be explained by
426 the recycling of trench sediments as has been done for several arc lavas (e.g. Mariana lavas
427 [*Bellot et al.*, 2018; *Elliott et al.*, 1997; *Hole et al.*, 1984]). Magmatic processes (e.g. partial
428 melting and/or fractional crystallization) are able to generate very small cerium depletion relative
429 to its neighboring elements [*Bellot et al.*, 2018] but cannot explain the lowest Ce/Ce* values
430 calculated for Gough samples. Moreover, Gough lavas do not show any correlation between their
431 elemental cerium anomaly and geochemical proxy of crystallization (e.g. MgO, Figure 7) or
432 trace-element ratios commonly used to identify magmatic processes.

433 Negative, elemental cerium anomalies are confirmed for 3 Gough samples. *Stracke* [2012]
434 described a potential effect of alteration on the Ce/Ce* for rare samples from Gough and Tristan
435 da Cunha Islands having very abnormal Ce/Ce* values lower than 0.85. For all other samples
436 from these two islands Ce/Ce* do not correlate with any geochemical proxy and thus no
437 indication of a likely alteration effect is identified. Depletion in cerium relative to other REE has
438 been described in very specific climatic condition (tropical environment, *Cotten et al.* [1995])

439 that are not applicable to the Gough Island. Weathering effects on REE elements are discussed in
440 detail in *Class and le Roex* [2008]: they are excluded to explain Ce/Ce* values measured in
441 Gough Island samples. A shallow-level contamination by local sediments having low Ce/Ce*
442 values is also ruled out because Ce/Ce* are not correlated to Ce/Pb ratios. Finally, seawater has a
443 highly negative Ce/Ce* but a very low Ce content (pmol/kg) in comparison to Gough lavas (Ce
444 = 95ppm). Thus, interaction with or exposition to seawater would not modify the REE pattern.

445 Negative, elemental cerium anomalies are reported in subcontinental lithospheric material
446 including kimberlites and lamproites from different locations (e.g. lamproites from Anatolia or
447 Western Australia [*Prelevic et al.*, 2012; *Fraser et al.*, 1985] and kimberlites from Lac de Gras
448 area, central Slave craton, Canada [*Tappe et al.*, 2013]). Samples from the GEOROC database
449 considered in this study are those for which all REE and both ^{147}Sm - ^{143}Nd and ^{176}Lu - ^{177}Hf
450 systematics were measured. The calculation of the elemental cerium anomaly is not trivial since
451 the different equations used in the calculation (using La-Pr or La-Nd with an exponential or a
452 linear interpolation) may give different results (up to 0.1) for samples characterized by very
453 strong enrichment in LREE relative to MREE. Amongst samples considered in Figure 6,
454 negative Ce/Ce* anomalies are commonly reported in lamproites from Anatolia [*Prelevic et al.*,
455 2012] and in samples from Leucite Hills [*Mirnejad and Bell*, 2006]. Swartruggens kimberlites
456 have the lowest Ce/Ce* amongst samples from the Group II kimberlites with values down to
457 0.91 when they are calculated using La and Nd. It seems therefore possible to produce small,
458 elemental cerium anomalies with the involvement of subcontinental lithospheric material in the
459 source of Gough samples.

460

461 **5 Conclusions**

462 Here we present the first measurements of the La-Ce isotope systematics in a series of lavas
463 coming from Gough Island, Atlantic Ocean. The samples have isotope signatures characteristic
464 of the EM-1 source component and they also present Ce/Ce* down to 0.93. Modelling a
465 primitive mantle source contaminated by 0.4 to 2.2% of a pelagic component is able to reproduce
466 the lowest Ce/Ce* values. However, the cerium isotope measurements show $\epsilon^{138}\text{Ce}$ values
467 between -0.39 and 0.15, too low to give support to the incorporation of recycled pelagic
468 sediments in the mantle source of the lavas. Modelled isotope compositions reach values
469 comprised between 1 and 4 $\epsilon^{138}\text{Ce}$ -units for a FOZO source contaminated by different proportion
470 (0.4 to 2.2%) of 2.5 Ga-old recycled sedimentary material. In a three-component mixture (OC-
471 sediments-FOZO), the calculated isotope compositions are less radiogenic (0.5 to 2.8 $\epsilon^{138}\text{Ce}$ -
472 units) and the sedimentary proportion varies from 1.4 to 4%. The near constancy of $\epsilon^{138}\text{Ce}$ values
473 of Gough samples characterized by variable Ce/Ce* does not agree with any type of pelagic
474 material mixing. Ce-Nd-Hf isotope compositions of Gough samples are more consistent with the
475 contribution in proportions between 10 and 30% of subcontinental lithospheric material in the
476 genesis of the EM-1 component. This scenario also explains both the negative $\Delta\epsilon\text{Hf}$ measured in
477 Gough Island samples, an isotope signature more commonly recorded in lamproites and Group II
478 kimberlites, and the slow, shallow seismic velocities identified for the Tristan da Cunha - Gough
479 hotspot.

480

481 **Acknowledgments**

482 All the new data are available in the main text. The GEOROC database is used for other
483 samples presented in the figure 6 (<http://georoc.mpch-mainz.gwdg.de/georoc/>). Anton the Roex
484 is warmly thanked for giving us the samples and for his constructive reading of the manuscript.
485 The help of Jean-Luc Piro and Mhammed Benbakkar with the mass spectrometers is gratefully
486 acknowledged. We thank Marion Garçon for all her advice in the chemistry lab. We thank the
487 Geological Survey of Japan for providing the isotopic standard JNdi-1. This work has further
488 benefited from comments by Jasper Konter and Bill White and an anonymous reviewer. This
489 project has received funding from the European Research Council (ERC) under the European
490 Union's Horizon 2020 research and innovation programme (Grant Agreement No 682778 -
491 ISOREE). This is a Laboratory of Excellence ClerVolc contribution no. XX.

492

493 **References**

- 494 Abouchami, W., A. W. Hofmann, S. J. G. Galer, F. A. Frey, J. Eisele, and M. Feigenson (2005),
495 Lead isotopes reveal bilateral asymmetry and vertical continuity in the Hawaiian mantle
496 plume, *Nature*, *434*, 851-856.
- 497 Barrat, J. A., B. Zanda, F. Moynier, C. Bollinger, C. Liorzou, and G. Bayon (2012),
498 Geochemistry of CI chondrites: Major and trace elements, and Cu and Zn isotopes,
499 *Geochim. Cosmochim. Acta*, *83*, 79-92.
- 500 Becker, M., and A. P. le Roex (2005), Geochemistry of South African on-and off-craton, Group I
501 and Group II kimberlites: petrogenesis and source region evolution, *J. Petrol.*, *47*, 673-703.

- 502 Bellot, N., M. Boyet, R. Doucelance, C. Pin, C. Chauvel, and D. Auclair (2015), Ce isotope
503 systematics of island arc lavas from the Lesser Antilles, *Geochim. Cosmochim. Acta*, *168*,
504 261-279.
- 505 Bellot, N., M. Boyet, R. Doucelance, P. Bonnand, I. P. Savov, T. Plank, and T. Elliott (2018),
506 Origin of negative cerium anomalies in subduction-related volcanic samples: Constraints
507 from Ce and Nd isotopes, *Chem. Geol.*, *500*, 46-63.
- 508 Blichert-Toft, J., F. A. Frey, and F. Albarède (1999), Hf isotope evidence for pelagic sediments
509 in the source of Hawaiian basalts, *Science*, *285*, 879-882.
- 510 Bonnand, P., C. Israel, M. Boyet, R. Doucelance, and D. Auclair (2019), Radiogenic and stable
511 Ce isotopes measurements by thermal ionisation mass spectrometry, *J. Anal. At. Spectrom.*,
512 *34*, 504-516.
- 513 Boschi, L., T. W. Becker, and B. Steinberger (2007), Mantle plumes: Dynamic models and
514 seismic images, *Geochem. Geophys. Geosyst.*, *8*, Q10006, doi:10.1029/2007GC001733.
- 515 Bouvier, A., J. D. Vervoort, and P. J. Patchett (2008), The Lu–Hf and Sm–Nd isotopic
516 composition of CHUR: constraints from unequilibrated chondrites and implications for the
517 bulk composition of terrestrial planets, *Earth Planet. Sci. Lett.*, *273*, 48-57.
- 518 Cabral, R. A., M. G. Jackson, E. Rose-Koga, K. Koga, M. J. Whitehouse, M. A. Antonelli, J.
519 Farquhar, J. M. D. Day, and E. H. Hauri (2013), Anomalous sulphur isotopes in plume
520 lavas reveal deep mantle storage of Archaean crust, *Nature*, *496*, 490-494.
- 521 Carlson, R. W., S. Esperanca, and D. P. Svisero (1996), Chemical and Os isotopic study of
522 Cretaceous potassic rocks from southern Brazil, *Contrib. Mineral. Petrol.*, *125*, 393-405.

- 523 Carlson, R. W., G. Czamanske, V. Fedorenko, and I. Ilupin (2006), A comparison of Siberian
524 meimechites and kimberlites: Implications for the source of high-Mg alkalic magmas and
525 flood basalts, *Geochem. Geophys. Geosyst.*, 7, Q11014, doi:10.1029/2006GC001342.
- 526 Castillo, P. R. (2015), The recycling of marine carbonates and sources of HIMU and FOZO
527 ocean island basalts, *Lithos*, 216, 254-263.
- 528 Chakrabarti, R., A. R. Basu, and D. K. Paul (2007), Nd–Hf–Sr–Pb isotopes and trace element
529 geochemistry of Proterozoic lamproites from southern India: Subducted komatiite in the
530 source, *Chem. Geol.*, 236, 291–302.
- 531 Chauvel, C., A. W. Hofmann, and P. Vidal (1992), HIMU-EM: the French Polynesian
532 connection, *Earth Planet. Sci. Lett.*, 110, 99-119.
- 533 Chauvel, C., S. Bureau, and C. Poggi (2011), Comprehensive chemical and isotopic analyses of
534 basalt and sediment reference materials, *Geostand. Geoanal. Res.*, 35, 125–143.
- 535 Class, C., and A. P. le Roex (2006), Continental material in the shallow oceanic mantle - how
536 does it get there?, *Geology*, 34, 129-132.
- 537 Class, C., and A. P. le Roex (2008), Ce anomalies in Gough Island lavas - trace element
538 characteristics of a recycled sediment component, *Earth Planet. Sci. Lett.*, 265, 475-486.
- 539 Coe, N., A. le Roex, J. Gurney, D. G. Pearson, and G. Nowell (2008), Petrogenesis of the
540 Swartruggens and Star Group II kimberlite dyke swarms, South Africa: constraints from
541 whole rock geochemistry, *Contrib. Mineral. Petrol.*, 156, 627-652.
- 542 Cotten, J., A. Le Dez, M. Bau, M. Caroff, R. C. Maury, P. Dulski, S. Fourcade, M. Bohn, and R.
543 Brousse (1995), Origin of anomalous rare-earth element and yttrium enrichments in
544 subaerially exposed basalts: evidence from French Polynesia, *Chem. Geol.*, 119, 115-138.

- 545 Courtillot, V., A. Davaille, J. Besse, and J. Stock (2003), Three distinct types of hotspots in the
546 Earth's mantle, *Earth Planet. Sci. Lett.*, *205*, 295-308.
- 547 Davies, G. R., A. J. Stolz, I. L. Mahotkin, G. M. Nowell, and D. G. Pearson (2006), Trace
548 element and Sr-Pb-Nd-Hf isotope evidence for ancient, fluid-dominated enrichment of the
549 source of the Aldan shield lamproites, *J. Petrol.*, *47*, 1119-1146.
- 550 Delavault, H., C. Chauvel, E. Thomassot, C. W. Devey, and B. Dazas (2016), Sulfur and lead
551 isotopic evidence of relic Archean sediments in the Pitcairn mantle plume, *Proc. Natl.*
552 *Acad. Sci.*, *113*, 12952-12956.
- 553 DePaolo, D. J. (1981), A Neodymium and Strontium Isotopic Study of the Mesozoic Calc-
554 Alkaline Granitic Batholiths of the Sierra Nevada and Peninsular Ranges, California, *J.*
555 *Geophys. Res.*, *86*, 10470-10488.
- 556 Derry, L. A., and S. B. Jacobsen (1988), The Nd and Sr isotopic evolution of Proterozoic
557 seawater, *Geophys. Res. Lett.*, *15*, 397-400.
- 558 Donnelly, C. L., W. L. Griffin, S. Y. O'Reilly, N. J. Pearson, and S. R. Shee (2011), The
559 Kimberlites and related rocks of the Kuruman Kimberlite Province, Kaapvaal Craton,
560 South Africa, *Contrib. Mineral. Petrol.*, *161*, 351-371.
- 561 Doucelance, R., N. Bellot, M. Boyet, T. Hammouda, and C. Bosq (2014), What coupled cerium
562 and neodymium isotopes tell us about the deep source of oceanic carbonatites, *Earth*
563 *Planet. Sci. Lett.*, *407*, 175-186.
- 564 Eisele, J., M. Sharma, S. J. Galer, J. Blichert-Toft, C. W. Devey, and A. W. Hofmann (2002),
565 The role of sediment recycling in EM-1 inferred from Os, Pb, Hf, Nd, Sr isotope and trace
566 element systematics of the Pitcairn hotspot, *Earth Planet. Sci. Lett.*, *196*, 197-212.

- 567 Elderfield, H., and M. J. Greaves (1982), The rare earth elements in seawater, *Nature*, 296, 214-
568 219.
- 569 Elliott, T., T. Plank, A. Zindler, W. White, and B. Bourdon (1997), Element transport from slab
570 to volcanic front at the Mariana arc, *J. Geophys. Res., Solid Earth*, 102, 14991-15019.
- 571 Escrig, S., R. Doucelance, M. Moreira, and C. J. Allègre (2005), Os isotope systematics in Fogo
572 Island: Evidence for lower continental crust fragments under the Cape Verde Southern
573 Islands, *Chem. Geol.*, 219, 93-113.
- 574 Farnetani, C. G., and A. W. Hofmann (2009), Dynamics and internal structure of a lower mantle
575 plume conduit, *Earth Planet. Sci. Lett.*, 282, 314-322.
- 576 Fraser, K. J., C. J. Hawkesworth, A. J. Erlank, R. H. Mitchell, and B. H. Scott-Smith (1985), Sr,
577 Nd and Pb isotope and minor element geochemistry of lamproites and kimberlites, *Earth
578 Planet. Sci. Lett.*, 76, 57-70.
- 579 French, S. W., and B. Romanowic (2015), Broad plumes rooted at the base of the Earth's mantle
580 beneath major hotspots, *Nature*, 525, 95-99.
- 581 Garçon, M., M. Boyet, R. W. Carlson, M. F. Horan, D. Auclair, and T. D. Mock (2018), Factors
582 influencing the precision and accuracy of Nd isotope measurements by thermal ionization
583 mass spectrometry, *Chem. Geol.*, 476, 493-514.
- 584 Grand, S. P., R. D. van der Hilst, and S. Widiyantoro (1997), High resolution global tomography:
585 a snapshot of convection in the Earth, *Geol. Soc. Am. TODAY*, 7.
- 586 Harris, C., H. S. Smith, and A. P. le Roex (2000), Oxygen isotope composition of phenocrysts
587 from Tristan da Cunha and Gough Island lavas: variation with fractional crystallization and
588 evidence for assimilation, *Contrib. Mineral. Petrol.*, 138, 164-175.

- 589 Hauri, E. H., and S. R. Hart (1993), Re-Os isotope systematics of HIMU and EMII oceanic
590 island basalts from the South Pacific Ocean, *Earth Planet. Sci. Lett.*, *114*, 353-371.
- 591 Hauri, E. H., and S. R. Hart (1997), Rhenium abundances and systematics in oceanic basalts,
592 *Chem. Geol.*, *139*, 185-205.
- 593 Hawkesworth, C. J., M. S. M. Mantovani, P. N. Taylor, and Z. Palacz (1986), Evidence from the
594 Parana of south Brazil for a continental contribution to Dupal basalts, *Nature*, *322*, 356-
595 359.
- 596 Hofmann, A. W. (1988), Chemical differentiation of the Earth: the relationship between mantle,
597 continental crust, and oceanic crust, *Earth Planet. Sci. Lett.*, *90*, 297-314.
- 598 Hofmann, A. W., and W. M. White (1982), Mantle plumes from ancient oceanic crust, *Earth*
599 *Planet. Sci. Lett.*, *57*, 421-436.
- 600 Hole, M., A. Saunders, G. Marriner, and J. Tarney (1984), Subduction of Pelagic Sediments -
601 Implications for the Origin of Ce-Anomalous Basalts From the Mariana Islands, *J. Geol.*
602 *Soc.*, *141*, 453-472.
- 603 Hoernle, K., J. Rohde, F. Hauff, D. Garbe-Schönberg, S. Homrighausen, R. Werner and J. P.
604 Morgan (2015). How and when plume zonation appeared during the 132 Myr evolution of
605 the Tristan Hotspot. *Nat. Commun.*, *6*, 7799.
- 606 Jackson, M. G., T.W. Becker, and J. G. Konter (2018), Evidence for a deep mantle source for
607 EM and HIMU domains from integrated geochemical and geophysical constraints, *Earth*
608 *Planet. Sci. Lett.*, *484*, 157-167.
- 609 Johnson, C. M., and B. L. Beard (1993), Evidence from hafnium isotopes for ancient sub-oceanic
610 mantle beneath the Rio Grande rift, *Nature* *362*, 441-444.

- 611 Kamber, B. S., and G. E. Webb (2001), The geochemistry of Late Archaean microbial carbonate:
612 implications for ocean chemistry and continental erosion history, *Geochim. Cosmochim.*
613 *Acta*, 65, 2509-2525.
- 614 Konter, J. G., and T. W. Becker (2012), Shallow lithospheric contribution to mantle plumes
615 revealed by integrating seismic and geochemical data, *Geochem. Geophys. Geosyst.*, 13,
616 Q02004, doi:10.1029/2011GC003923.
- 617 Kurz, M. D., Jenkins, W. J., and Hart, S. R. (1982), Helium isotopic systematics of oceanic
618 islands and mantle heterogeneity. *Nature*, 297(5861), 43-47.
- 619 Le Maitre, R. W. (1962), Petrology of volcanic rocks, Gough Islands, South Atlantic, *Bull. Geol.*
620 *Soc. Am.*, 73, 1309-1340.
- 621 le Roex, A. P. (1985), Geochemistry, mineralogy and magmatic evolution of the basaltic and
622 trachytic lavas from Gough Island, South Atlantic, *J. Petrol.*, 26, 149-186.
- 623 le Roex, A. P., R. A. Cliff, and B. J. I. Adair (1990), Tristan da Cunha, South Atlantic:
624 Geochemistry and Petrogenesis of a Basanite-Phonolite Lava Series, *J. Petrol.*, 31, 779-
625 812.
- 626 Longerich, H. P. (1993), Oxychlorine ions in inductively coupled plasma mass spectrometry:
627 effect of chlorine speciation as Cl^- and ClO_4^- , *J. Anal. At. Spectrom.*, 8, 439-444.
- 628 McDonough, W. F., and S. S. Sun (1995), The composition of the Earth, *Chem. Geol.*, 120, 223-
629 253.
- 630 McKenzie, D., and R. K. O'Nions (1991), Partial melt distributions from inversion of rare Earth
631 element concentrations, *J. Petrol.*, 32, 1,021-1,091.
- 632 Mirnejad, H., and K. Bell (2006), Origin and Source Evolution of the Leucite Hills Lamproites:
633 Evidence from Sr–Nd–Pb–O Isotopic Compositions, *J. Petrol.*, 47, 2463-2489.

- 634 Nowell, G. M., D. G. Pearson, D. R. Bell, R. W. Carlson, C. B. Smith, P. D. Kempton, and S. R.
635 Noble (2004), Hf Isotope Systematics of Kimberlites and their Megacrysts: New
636 Constraints on their Source Regions, *J. Petrol.*, *45*, 1583-1612.
- 637 O'Connor, J. M., and W. Jokat (2015), Tracking the Tristan-Gough mantle plume using discrete
638 chains of intraplate volcanic centers buried in the Walvis ridge, *Geology*, *43*, 715-718.
- 639 Patino, L. C., M. J. Carr, and M. D. Feigenson (2000), Local and regional variations in Central
640 American arc lavas controlled by variations in subducted sediment input, *Contrib. Mineral.*
641 *Petrol.*, *138*, 265-283.
- 642 Plank, T. (2013), The chemical composition of subducting sediments, In: *Treatise on*
643 *Geochemistry: Second Edition*, 2nd ed. Elsevier Ltd., [https://doi.org/10.1016/B978-0-08-](https://doi.org/10.1016/B978-0-08-095975-7.00319-3)
644 [095975-7.00319-3](https://doi.org/10.1016/B978-0-08-095975-7.00319-3).
- 645 Pourmand, A., N. Dauphas, and T. J. Ireland (2012), A novel extraction chromatography and
646 MC-ICP-MS technique for rapid analysis of REE, Sc and Y: Revising CI-chondrite and
647 Post-Archean Australian Shale (PAAS) abundances, *Chem. Geol.*, *291*, 38-54.
- 648 Prelevic, D., C. Akal, S. F. Foley, R. L. Romer, A. Stracke, and P. Van den Bogaard (2012),
649 Ultrapotassic Mafic Rocks as Geochemical Proxies for Post-collisional Dynamics of
650 Orogenic Lithospheric Mantle: the Case of Southwestern Anatolia, Turkey, *J. Petrol.*, *53*,
651 1019-1055.
- 652 Riding, R., P. Fralick, and L. Liang (2014), Identification of an Archean marine oxygen oasis,
653 *Precambrian Res.*, *251*, 232-237.
- 654 Rohde J. K., P. van den Bogaard, K. Hoernle, F. Hauff, and R. Werner (2013), Evidence for an
655 age progression along the Tristan-Gough volcanic track from new $^{40}\text{Ar}/^{39}\text{Ar}$ ages on
656 phenocryst phases, *Tectonophysics*, *604*, 60-71.

- 657 Rizo, H., M. Boyet, J. Blichert-Toft, and M. T. Rosing (2011), Combined Nd and Hf isotope
658 evidence for deep-seated source of Isua lavas, *Earth Planet. Sci. Lett.*, *312*, 267-279.
- 659 Salters, V. J. M., and S. R. Hart (1991), The mantle sources of ocean ridges, islands and arcs: the
660 Hf-isotope connection, *Earth Planet. Sci. Lett.*, *104*, 364-380.
- 661 Salters, V. J., S. Mallick, S. R. Hart, C. E. Langmuir and A. Stracke (2011), Domains of depleted
662 mantle: New evidence from hafnium and neodymium isotopes. *Geochemistry, Geophysics,*
663 *Geosystems*, *12*(8), Q08001, doi:10.1029/2011GC003617.
- 664 Satkoski, A. M., P. Fralick, B. L. Beard, and C. M. Johnson (2017), Initiation of modern-style
665 plate tectonics recorded in Mesoarchean marine chemical sediments, *Geochim.*
666 *Cosmochim. Acta*, *209*, 216-232.
- 667 Schwindrofska, A., K. Hoernle, F. Hauff,, P. van den Bogaard,, R. Werner, and D. Garbe-
668 Schönberg (2016), Origin of enriched components in the South Atlantic: Evidence from 40
669 Ma geochemical zonation of the Discovery Seamounts. *Earth Planet. Sci. Lett.*, *441*, 167-
670 177.
- 671 Smith, C. B. (1983), Pb, Sr and Nd isotopic evidence for sources of southern African Cretaceous
672 kimberlites, *Nature*, *304*, 51-54.
- 673 Smith, C. B., J. J. Gurney, E. M. W. Skinner, C. R. Clement, and N. Ebrahim (1985),
674 Geochemical character of southern African kimberlites: a new approach based on isotopic
675 constraints, *Trans. Geol. Soc. South Africa*, *88*, 267-280.
- 676 Stracke, A. (2012), Earth's heterogeneous mantle: a product of convection-driven interaction
677 between crust and mantle, *Chem. Geol.*, *330*, 274-299.
- 678 Stracke, A., A. W. Hofmann, and S. R. Hart (2005), FOZO, HIMU, and the rest of the mantle
679 zoo, *Geochem. Geophys. Geosyst.*, *6*, Q05007, doi:10.1029/2004GC000824.

- 680 Tackley, P. J. (2015), Mantle Geochemical Geodynamics, *Treatise on Geophysics*, 7, 521-585
681 second edition. Elsevier B.V.
- 682 Tanimizu, M. (2000), Geophysical determination of the ^{138}La λ -decay constant, *Phys. Rev.*, *62*,
683 140-143.
- 684 Tappe, S., D. G. Pearson, B. A. Kjarsgaard, G. Nowell, and D. Dowall (2013), Mantle transition
685 zone input to kimberlite magmatism near a subduction zone: origin of anomalous Nd–Hf
686 isotope systematics at Lac de Gras, Canada, *Earth Planet. Sci. Lett.*, *371*, 235-251.
- 687 Tazoe, H., H. Obata, and T. Gamo (2007), Determination of cerium isotope ratios in
688 geochemical samples using oxidative extraction technique with chelating resin, *J. Anal. At.*
689 *Spectrom.*, *22*, 616-622.
- 690 van der Hilst, R. D., S. Widiyantoro, and E. R. Engdahl (1997), Evidence for deep mantle
691 circulation from global tomography, *Nature*, *386*, 578-584.
- 692 Van Kranendonk, M., G. E. Webb, and B. S. Kamber (2003), Geological and trace evidence for a
693 marine sedimentary environment of deposition and biogenicity of 3.45 Ga stromatolitic
694 carbonates in the Pilbara Craton, and support for a reducing Archaean ocean, *Geobiology*,
695 *1*, 91-108.
- 696 Vervoort, J. D., T. Plank, and J. Prytulak (2011), The Hf-Nd isotopic composition of marine
697 sediments, *Geochim. Cosmochim. Acta*, *75*, 5903-5926.
- 698 Weaver, B. L., D. A. Wood, J. Tarney, and J.-L. Joron (1986), Role of subducted sediment in the
699 genesis of ocean-island basalts: geochemical evidence from South Atlantic Ocean islands,
700 *Geology*, *14*, 275-278.
- 701 Weaver, B. L. (1991), The origin of ocean island basalt end-member compositions: Trace element
702 and isotopic constraints, *Earth Planet. Sci. Lett.*, *104*, 381-397.

- 703 Weis, D., M. O. Garcia, J. M. Rhodes, M. Jellinek, and J. S. Scoates (2011), Role of the deep
704 mantle in generating the compositional asymmetry of the Hawaiian mantle plume, *Nature*
705 *Geosci.*, *4*, 831-838.
- 706 Willbold, M., and A. Stracke (2006), Trace element composition of mantle end-members:
707 Implications for recycling of oceanic and upper and lower continental crust, *Geochem.*
708 *Geophys. Geosyst.*, *7*, Q04004, DOI: 10.1029/2005GC001005.
- 709 Willig, M., and A. Stracke (2018), Accurate and precise measurement of Ce isotope ratios by
710 thermal ionization mass spectrometry (TIMS), *Chem. Geol.*, *476*, 119–129.
- 711 Willig, M., and A. Stracke (2019), Earth's chondritic light rare earth element composition:
712 Evidence from the Ce–Nd isotope systematics of chondrites and oceanic basalts, *Earth*
713 *Planet. Sci. Lett.*, *509*, 55-65.
- 714 White, W. M., and A. W. Hofmann (1982), Sr and Nd isotope geochemistry of oceanic basalts
715 and mantle evolution, *Nature*, *296*, 821-825.
- 716 Zindler, A., and S. R. Hart (1986), Chemical geodynamics, *Ann. Rev. Earth Planet. Sci.*, *14*, 493-
717 571.
- 718
- 719

720 **Figure 1.** Elemental cerium anomalies of Gough Island lavas. Square symbols correspond to samples analyzed in
 721 this study (LMV1 and LMV2) and also measured by *Class and le Roex* [2008] (noted C & LR 2008). The names of
 722 the samples are shown on the right-hand side of the figure. Circles refer to another set of samples analyzed by
 723 *Willbold and Stracke* [2006] (noted W & S 2006). The error is twice the average of the differences between the two
 724 LMV measurements (3.1 %).

725 **Figure 2.** Rare earth element patterns of Gough lavas (the concentrations are normalised to the CHUR values of
 726 *Pourmand et al.* [2012]).

727 **Figure 3.** Ce, Nd and Hf isotope composition of Gough Island lavas. A) ϵ_{Hf} vs. ϵ_{Nd} ; B) ϵ_{Nd} vs. ϵ_{Ce} ; C) ϵ_{Hf} vs.
 728 ϵ_{Ce} . Errors correspond to the analytical uncertainty (2SE).

729 **Figure 4.** Elemental cerium anomaly vs. ϵ_{Ce} values (error bars = 2SE) of Gough Island. The elemental cerium
 730 anomaly for each sample corresponds to the mean value determined in this study (LMV1 and LMV2 in Figure 1).
 731 Error on the elemental cerium anomaly is twice the average of the differences between the two LMV measurements
 732 (3.1 %).

733 **Figure 5.** Modelled Ce isotope compositions together with elemental cerium anomalies of a primitive mantle source
 734 (FOZO-like) contaminated by various amounts of a 2.5 Ga-old, «pelagic component» (proportions in percent are
 735 given in the diagrams). The 3 sedimentary reservoirs considered in the calculations are R1: mean composition of
 736 carbonate sediments from DSDP Site 495 [*Patino et al.*, 2000]; R2: Pacific Authigenic Weighted Mean sediments
 737 [*Hole et al.*, 1984]; and R3: average composition of material drilled in Kemadec, Tonga, Vanuatu, Marianas and
 738 Izu-Bonin trenches [*Plank*, 2013]. A) FOZO source + sediments; B) FOZO source + sediment melts derived by 25%
 739 partial melting of the sediment protolith; C) FOZO source + slab (sediments and oceanic crust in proportion 5:95).
 740 In this last case, we assume a productivity 10 times higher for sediments than for the mafic component (recycled
 741 oceanic crust -FOZO) during partial melting. More details on these reservoirs are given in the text and in Table 4.

742 **Figure 6.** A) $\epsilon_{\text{Hf}}-\epsilon_{\text{Nd}}$ of samples from Gough and Tristan da Cunha Islands. Data from *Salters et al.* [2011] and this
 743 study. B) $\epsilon_{\text{Hf}}-\epsilon_{\text{Nd}}$ isotope mixing models between a FOZO-like mantle source and sub-continental lithospheric
 744 material. Geochemical compositions of the reservoirs are reported in Table 4. Epsilon values are calculated using

745 CHUR data from *Bouvier et al.* [2008]. The mantle array is defined using the equation of *Vervoort et al.* [2011]: ϵHf
746 $= 1.55 \times \epsilon\text{Nd} + 1.21$. Data for South Africa Group II kimberlites: X007 from the Kuruman Kimberlite Province
747 [*Donnelly et al.*, 2011]), Finsch Mine [*Nowell et al.*, 2004; *Fraser et al.*, 1985]), Swartuggens [*Coe et al.*, 2008;
748 *Nowell et al.*, 2004; *Smith* 1983; *Smith et al.*, 1985], Star [*Coe et al.*, 2008]. Data for lamproites: Siberia [*Davies et*
749 *al.*, 2006], Dharwar [*Chakrabarti et al.*, 2007], Anatolia [*Prelevic et al.*, 2012], Leucite Hills from Wyoming, USA
750 [*Mirnejad and Bell*, 2006; *Salters and Hart*, 1991]. Mixing has been calculated using the average value of
751 Swartuggens kimberlites (South Africa, 150Ma). Since no lamproite comes from South Africa, the mean value is
752 calculated from the youngest samples that are those from Leucite Hills (0.9-3.1 Ma). Errors bars in panel are 2SD.
753 They are smaller than the symbol size in the panel B.

754 **Figure 7.** Cerium anomaly of Gough Island lavas as a function of the MgO content (wt. %). The elemental cerium
755 anomaly for each sample corresponds to the mean value determined in this study (LMV1 and LMV2 in Figure 1).
756 Error on the elemental cerium anomaly is twice the average of the differences between the two LMV measurements
757 (3.1 %).

Figure 1.

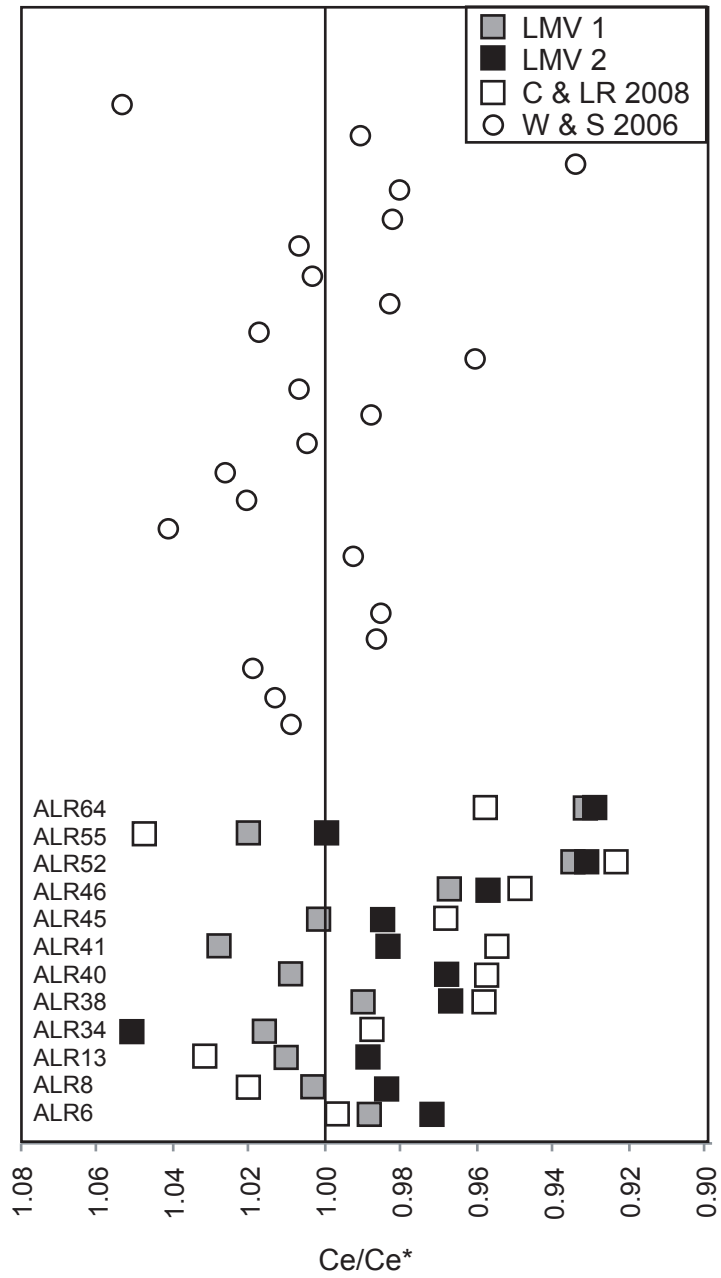


Figure 2.

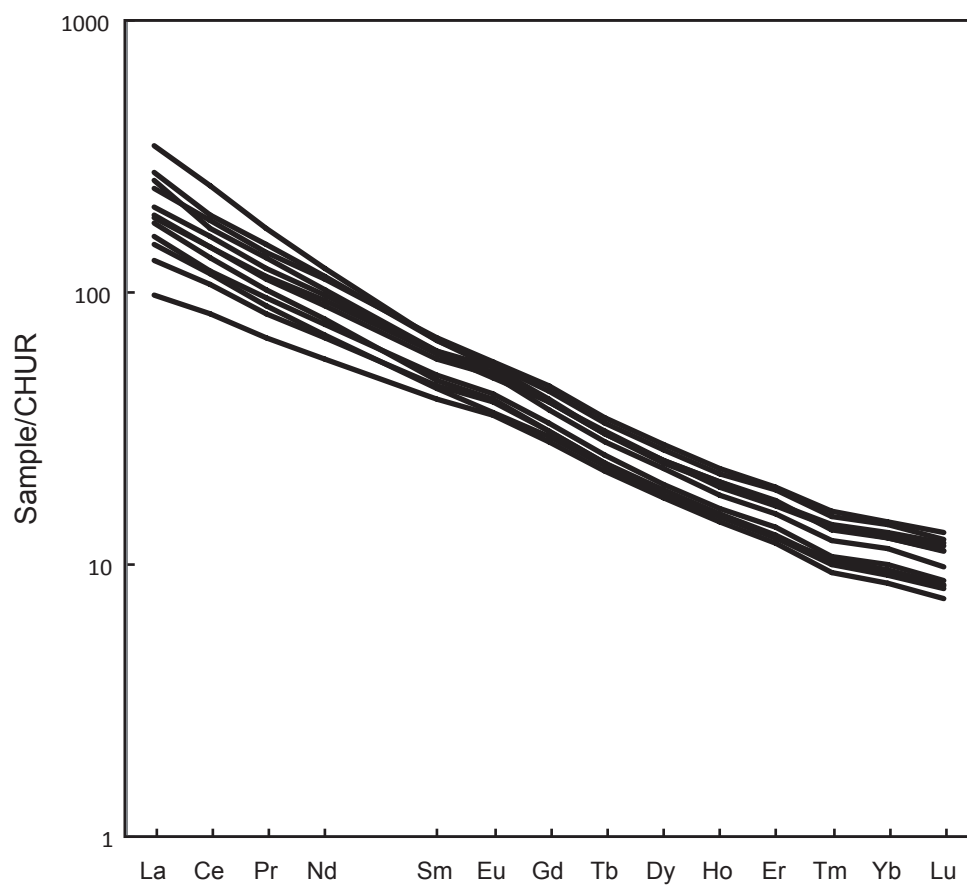


Figure 3.

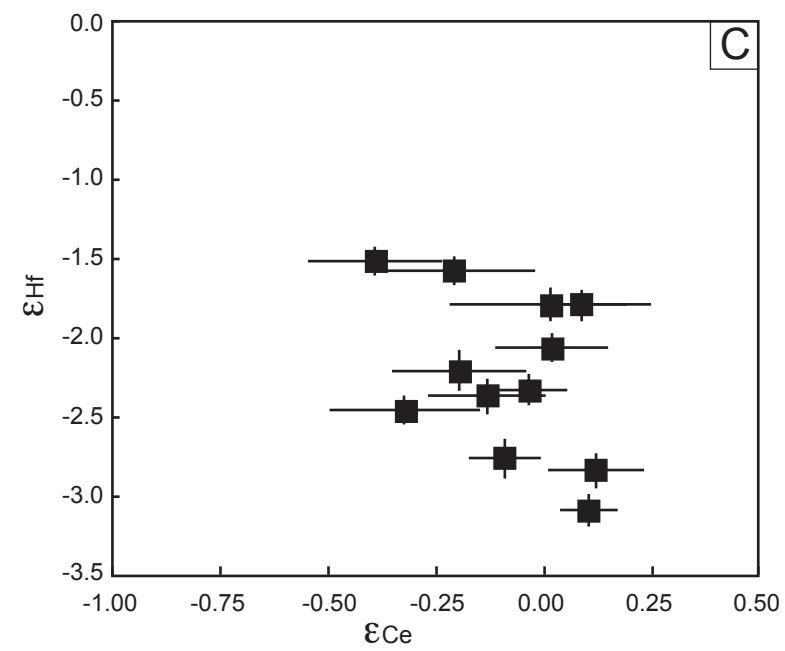
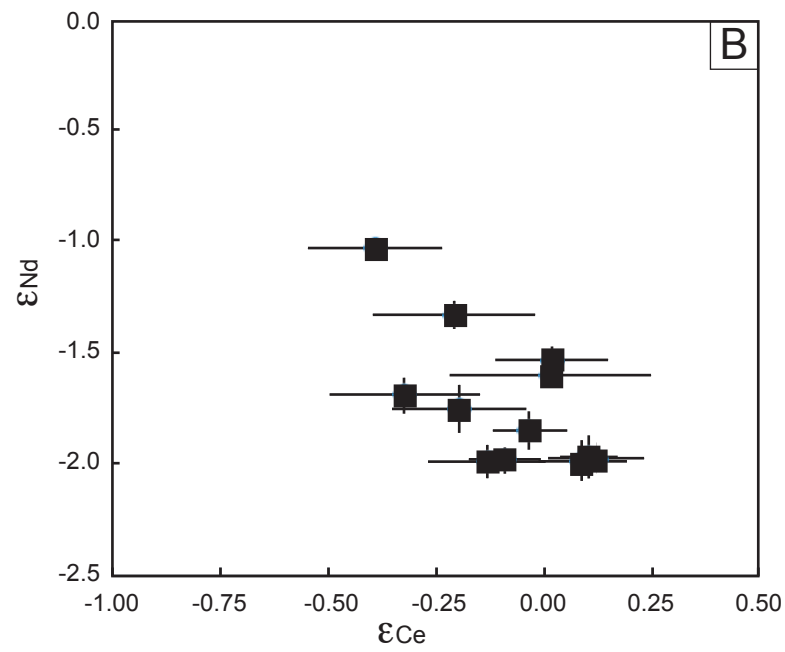
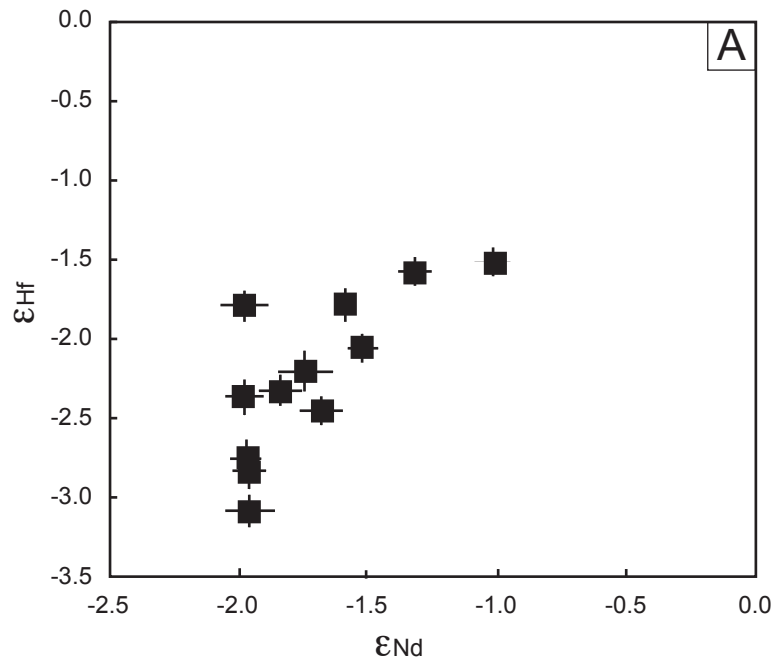


Figure 4.

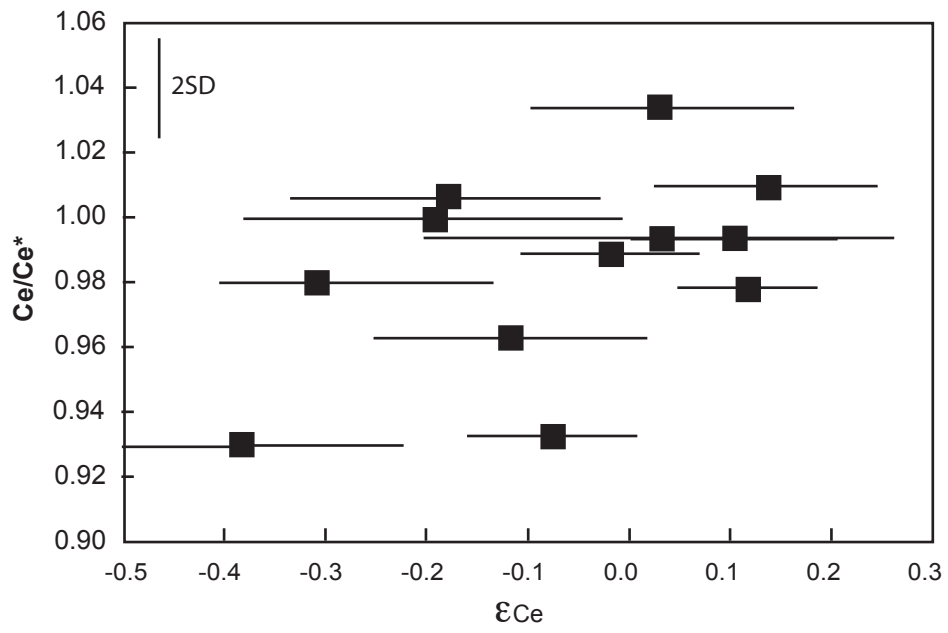


Figure 5.

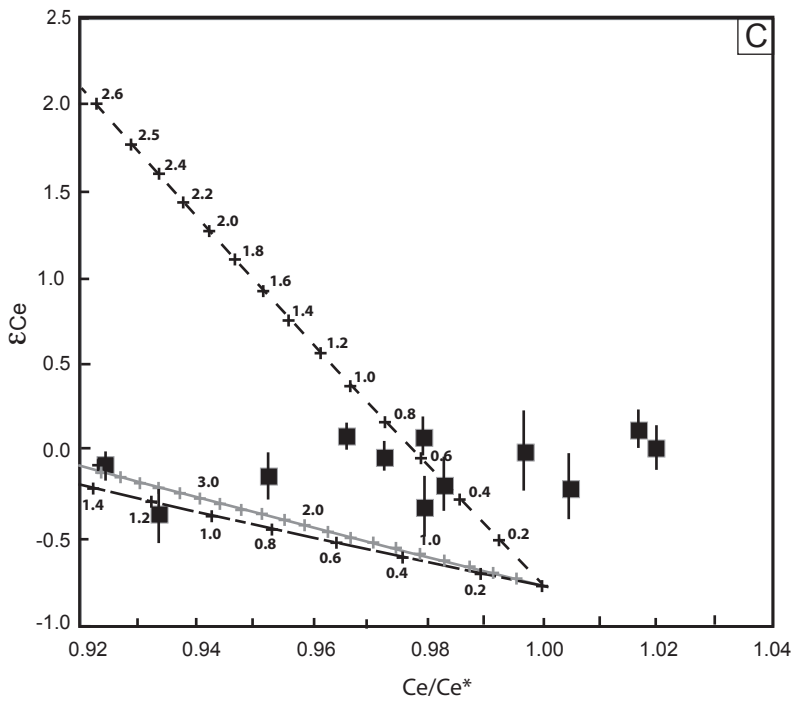
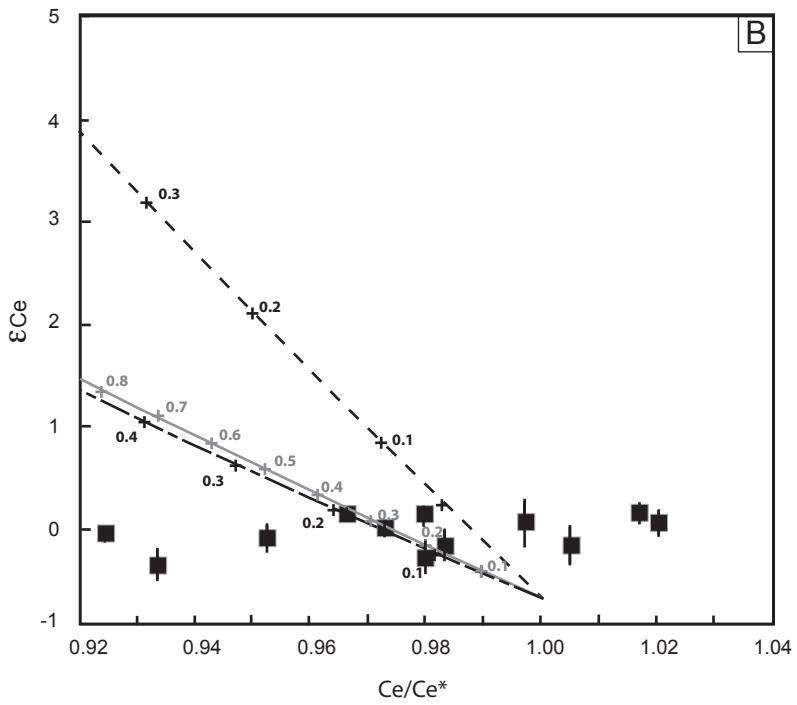
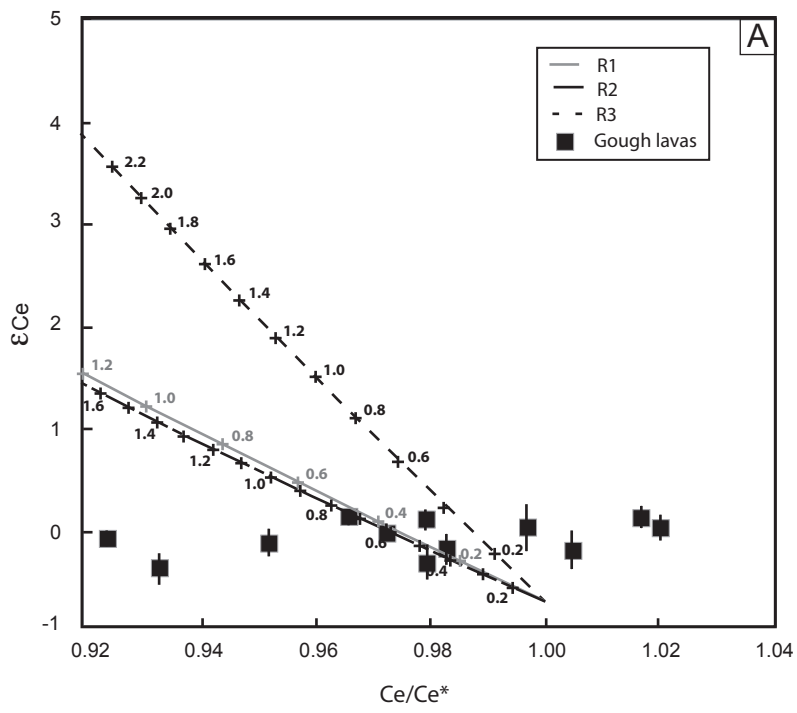


Figure 6.

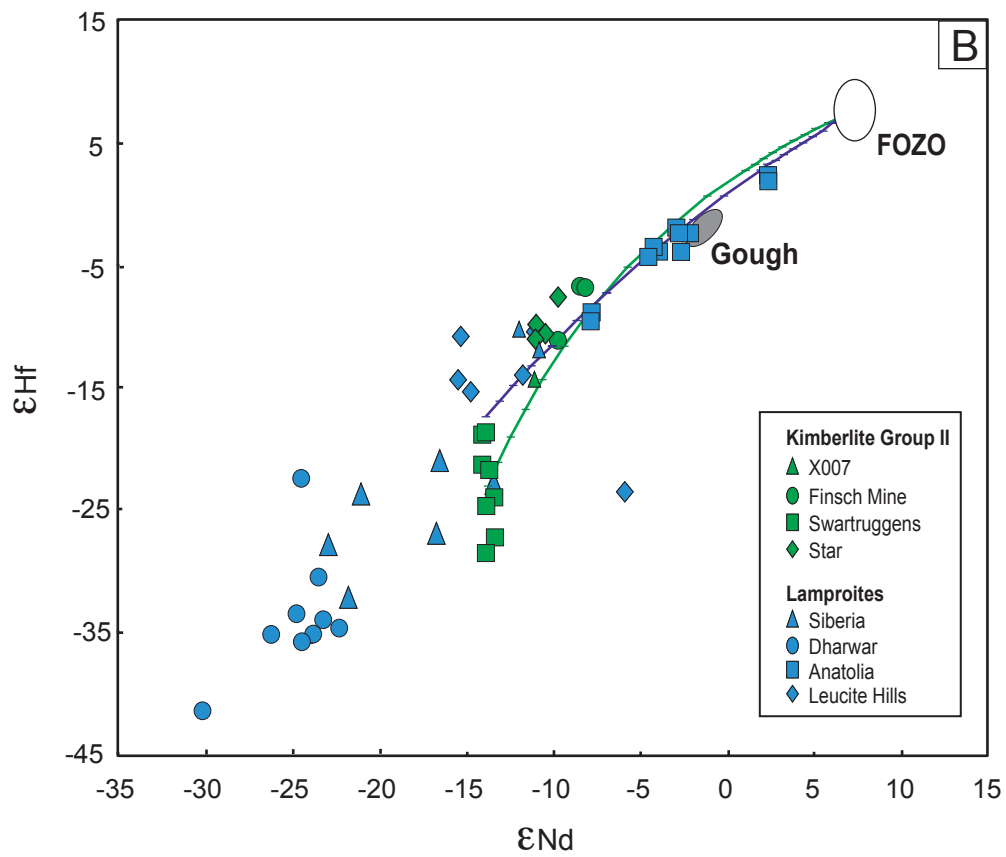
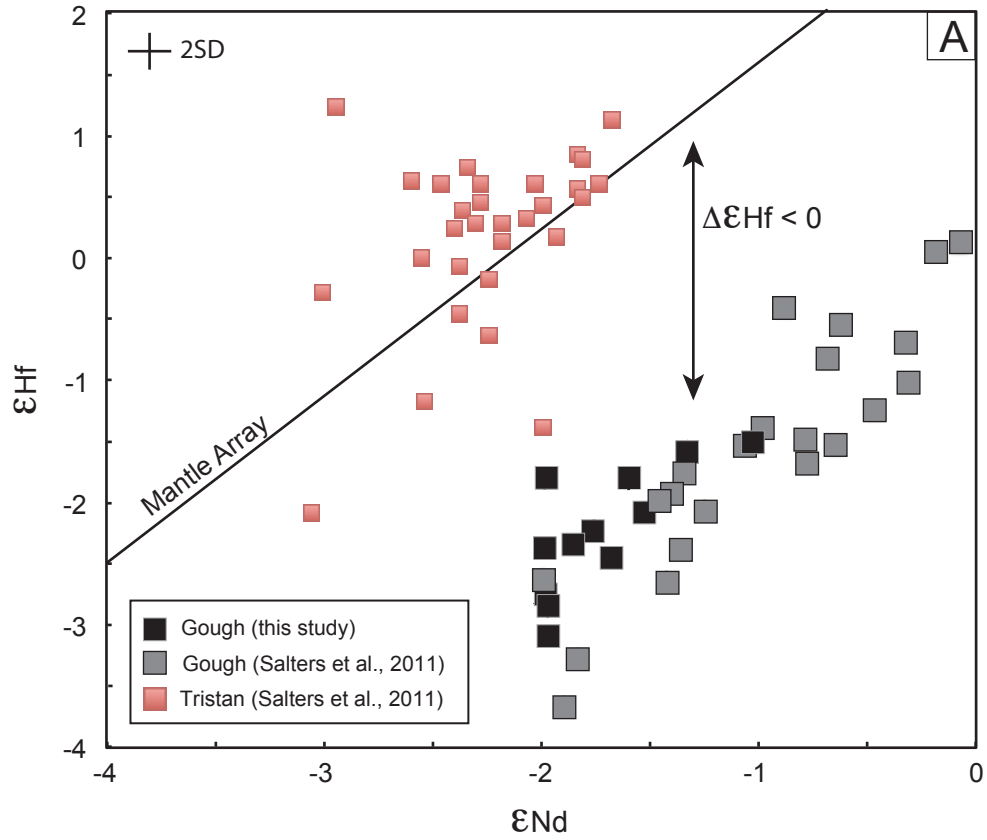


Figure 7.

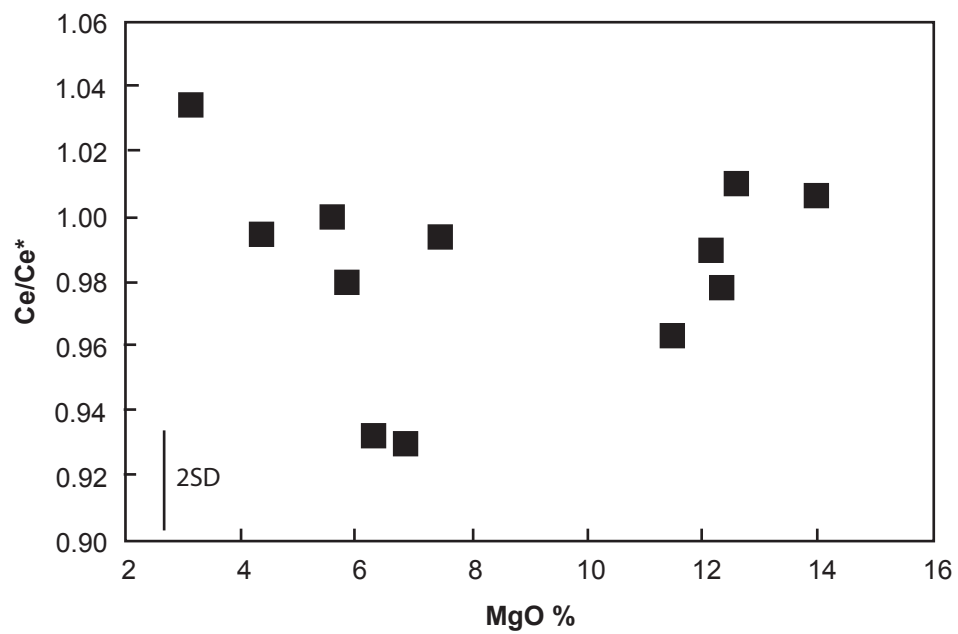


Table 1. Description of the different chemistry procedures applied for the cerium anomaly measurement of the rock standard BHVO-2 and their values expressed in % deviation.

# experiment	A	B	C	D	E	F	G	H	I	J	K
weight BHVO-2 (g)	0.0518	0.0498	0.0495	0.0498	0.0504	0.0502	0.0526	0.0496	0.05	0.0499	0.0507
step in HClO ₄	x	x	x	x	x						
volume solution (ml)	20	20	5	10	30	20	20	20	20	20	20
acid and molarity	HNO ₃ 7M	HNO ₃ 7M	HNO ₃ 7M	HNO ₃ 7M	HNO ₃ 7M	HNO ₃ 7M	HNO ₃ 7M	HCl 6M	HCl 6M	HCl 6M	HCl 6M
final dilution	3383.99	3507.01	3453.90	3449.18	3437.48	3476.23	3448.10	3594.34	3413.40	3433.97	3391.90
$\Delta\text{Ce}/\text{Ce}^*$ (%)	0.06	0.12	0.14	-0.30	-0.18	-0.04	-0.07	-0.17	-0.02	0.04	0.39

⁽¹⁾ $\Delta\text{Ce}/\text{Ce}^*$ (%) corresponds to the variation of the calculated cerium anomaly of BHVO-2 relative to its theoretical anomaly of 1.006 (GeoREM).

Table 2: Major- (%) and trace-element (ppm) contents of Gough Island lavas together with calculated cerium anomalies.

	ALR_6G	ALR_8G	ALR_13G	ALR_34G	ALR_38G	ALR_40G	ALR_41G	ALR_45G	ALR_46G	ALR_52G	ALR_55G	ALR_64G
	basalt	trachy-basalt	trachy-basalt	basaltic trachy -andesite	basalt	basalt	basalt	trachy-basalt	basalt	trachy-basalt	basalt	trachy-basalt
Latitude S	40° 20.25'	40° 20.25'	40° 20.25'	40° 19.2'	40° 20.1'	40° 20'	40° 20'	40° 20'	40° 20'	40° 20'	40° 19.3'	40° 19.2'
Longitude W	9° 53.5'	9° 52.8'	9° 52.8'	9° 52.8'	9° 52.8'	9° 55.1'	9° 55.1'	9° 55.1'	9° 55.1'	9° 55.2'	9° 55.5'	9° 55.5'
<i>Major element (%)</i>												
SiO ₂	48.80	48.88	49.00	51.09	47.04	48.18	48.61	48.25	48.21	49.71	47.35	50.00
Al ₂ O ₃	14.62	15.58	15.03	17.93	11.73	10.76	8.50	14.19	11.56	14.70	11.40	14.68
Fe ₂ O ₃	11.52	11.35	10.77	8.40	12.32	12.18	11.67	12.05	12.46	11.52	12.44	11.02
MgO	5.82	4.33	5.54	3.12	12.35	12.13	14.01	7.47	11.48	6.27	12.60	6.85
CaO	9.30	8.05	8.95	6.13	8.71	9.42	12.15	8.02	8.86	7.86	9.15	8.43
Na ₂ O	2.82	3.37	3.17	4.70	2.38	2.33	1.77	3.11	2.48	3.16	2.37	3.33
K ₂ O	1.81	2.57	2.56	3.98	1.92	1.62	1.22	2.20	1.80	2.96	1.77	2.48
TiO ₂	3.27	3.92	3.37	2.38	2.69	2.63	2.32	3.34	2.82	3.21	2.84	3.09
MnO	0.15	0.15	0.15	0.13	0.16	0.16	0.17	0.16	0.17	0.16	0.17	0.15
P ₂ O ₅	0.60	0.79	0.77	1.16	0.56	0.43	0.33	0.65	0.49	0.82	0.45	0.65
<i>Trace element (ppm)</i>												
Li	5.27	7.50	6.60	9.15	5.82	5.31	4.64	6.91	6.31	8.31	5.99	7.21
Be	1.39	1.76	1.47	2.56	1.13	1.01	0.80	1.38	1.30	1.90	1.25	1.69
Sc	27.94	22.30	23.57	10.90	25.06	28.92	41.28	22.11	28.65	21.29	27.47	21.51
V	247	257	228	150	193	215	257	206	225	227	213	206
Cr	140	28	129	5	504	747	1,388	219	635	184	553	192
Mn	1,252	1,161	1,122	957	1,229	1,245	1,289	1,232	1,322	1,262	1,300	1,214
Co	41.2	31.4	33.7	19.7	64.1	59.7	58.6	49.8	61.6	38.7	64.6	40.6
Ni	84.3	28.5	71.2	13.3	325.7	348.7	357.5	230.7	353.0	114.0	371.2	145.5
Cu	38.1	18.9	31.3	19.3	22.5	29.5	21.8	42.2	38.4	32.7	46.7	47.0
Zn	118	118	104	98	103	107	94	122	119	123	109	111
Ga	25.5	27.1	25.1	27.3	19.1	18.6	16.0	25.1	21.9	26.8	20.0	25.1
Ge	1.95	1.88	1.72	1.64	1.76	1.89	1.71	1.89	1.91	2.00	1.83	1.89
Rb	24.7	40.6	45.8	110.3	37.9	30.1	22.5	32.7	35.7	71.4	40.7	54.1
Sr	789	783	850	1,080	712	572	414	800	628	860	632	783
Y	30.9	34.0	29.2	29.1	23.2	23.2	21.7	28.0	25.3	34.1	22.9	32.5
Zr	286	351	295	461	242	218	169	298	256	364	241	321
Nb	43.8	65.1	57.6	98.0	38.1	31.7	23.7	45.9	36.7	70.9	39.3	61.1
Mo	1.81	2.30	2.32	3.33	1.70	1.69	1.57	1.71	1.73	2.05	2.16	1.97
Sn	2.23	2.42	2.06	2.51	1.76	1.60	1.34	2.07	1.71	2.59	1.79	2.16
Ba	609	752	791	1,088	637	516	376	744	587	900	592	792
La	46.9	59.1	50.7	85.6	44.4	32.5	24.2	47.2	39.9	68.1	36.7	64.1
Ce	91.7	116.1	101.2	156.7	84.6	67.0	52.9	92.9	75.7	120.4	74.6	109.2
Pr	10.9	13.4	11.7	16.5	9.7	8.0	6.5	10.8	9.1	14.4	8.6	12.7
Nd	45.1	53.9	47.8	60.1	38.7	33.3	27.7	43.7	37.3	55.9	34.2	49.6
Sm	9.30	10.58	9.53	10.42	7.45	7.06	6.31	8.84	7.64	10.39	6.90	9.39
Eu	2.94	3.34	3.20	3.19	2.43	2.35	2.10	2.96	2.55	3.22	2.19	3.05
Gd	8.32	9.40	8.31	8.40	6.42	6.46	5.89	7.80	6.94	9.12	6.16	8.38
Tb	1.15	1.31	1.14	1.15	0.88	0.89	0.83	1.07	0.95	1.26	0.87	1.16
Dy	6.28	7.03	6.16	6.10	4.64	4.87	4.52	5.75	5.11	6.74	4.66	6.18
Ho	1.11	1.26	1.08	1.08	0.82	0.85	0.80	1.00	0.89	1.20	0.82	1.11
Er	2.82	3.22	2.76	2.82	2.09	2.14	1.98	2.53	2.28	3.11	2.09	2.89
Tm	0.36	0.41	0.35	0.36	0.26	0.27	0.25	0.32	0.28	0.39	0.27	0.35
Yb	2.17	2.45	2.10	2.24	1.54	1.57	1.46	1.93	1.70	2.36	1.63	2.11
Lu	0.30	0.34	0.29	0.31	0.21	0.21	0.19	0.25	0.22	0.32	0.22	0.28
Hf	6.67	8.12	6.78	9.64	5.51	4.97	4.04	6.58	5.58	8.16	5.51	6.86
Ta	2.58	3.59	3.11	5.45	2.21	1.80	1.33	2.58	2.03	3.84	2.24	3.16
W	0.56	0.80	0.77	1.27	0.45	0.49	0.41	0.49	0.50	0.42	0.63	0.30
Pb	3.95	4.56	3.65	8.89	3.59	2.86	1.89	4.03	3.27	4.68	3.66	4.71
Th	4.31	5.97	5.38	12.22	4.01	3.07	2.21	4.29	3.46	7.16	3.99	5.65
U	0.70	1.10	1.09	2.44	0.70	0.59	0.43	0.74	0.72	1.38	0.77	1.15
Ce/Ce* LMV1	0.99	1.00	1.01	1.02	0.99	1.01	1.03	1.00	0.97	0.93	1.02	0.93
Ce/Ce* LMV2	0.97	0.98	0.99	1.05	0.97	0.97	0.98	0.96	0.96	0.93	1.00	0.93

Cerium anomalies are calculated using $Ce/Ce^* = (CeN / (LaN_{0.5} \times PrN_{0.5}))$ and considering CI-chondrite values from *Pourmand et al. [2012]* for normalization. Ce/Ce*LMV1 is calculated from the measurement of an aliquot uptaken before the chemical separation (calibration relative to a synthetic CMS solution). Ce/Ce*LMV2 is calculated from the measurement of a second dissolution (calibration with rock standard BHVO-2). See text for more details.

Table 3: $^{138}\text{Ce}/^{142}\text{Ce}$, $^{143}\text{Nd}/^{144}\text{Nd}$ and $^{176}\text{Hf}/^{177}\text{Hf}$ measured in Gough Island lavas.

Sample	$^{138}\text{Ce}/^{142}\text{Ce}$	2SE ⁽¹⁾	$\epsilon^{138}\text{Ce}$ ⁽²⁾	$^{143}\text{Nd}/^{144}\text{Nd}$	2SE ⁽¹⁾	$\epsilon^{143}\text{Nd}$ ⁽²⁾	$^{176}\text{Hf}/^{177}\text{Hf}$	2SE ⁽¹⁾	$\epsilon^{176}\text{Hf}$ ⁽²⁾
ALR6G	0.0225656	0.0000004	-0.32	0.512543	0.000004	-1.69	0.282716	0.000003	-2.45
ALR8G	0.0225664	0.0000005	0.02	0.512548	0.000002	-1.60	0.282734	0.000003	-1.79
ALR13G	0.0225659	0.0000004	-0.20	0.512562	0.000003	-1.33	0.282740	0.000003	-1.58
ALR34G	0.0225664	0.0000003	0.02	0.512552	0.000003	-1.53	0.282727	0.000003	-2.06
ALR38G	0.0225666	0.0000002	0.11	0.512529	0.000005	-1.97	0.282698	0.000003	-3.08
ALR40G	0.0225663	0.0000002	-0.03	0.512535	0.000004	-1.85	0.282719	0.000003	-2.33
ALR41G	0.0225659	0.0000003	-0.19	0.512540	0.000006	-1.76	0.282723	0.000004	-2.21
ALR45G	0.0225666	0.0000002	0.09	0.512528	0.000005	-1.99	0.282734	0.000003	-1.79
ALR46G	0.0225661	0.0000003	-0.13	0.512528	0.000004	-1.99	0.282718	0.000003	-2.37
ALR52Ga	0.0225661	0.0000002	-0.09	0.512528	0.000003	-1.98	0.282707	0.000004	-2.76
ALR55G	0.0225666	0.0000003	0.13	0.512529	0.000003	-1.97	0.282705	0.000003	-2.83
ALR64G	0.0225655	0.0000004	-0.39	0.512577	0.000004	-1.03	0.282742	0.000003	-1.52

⁽¹⁾Errors correspond to the analytical uncertainty (2SE).

⁽²⁾Epsilon values are calculated relative to CHUR data using the equation $\epsilon = (R_{\text{sample}}/R_{\text{CHUR}} - 1) \times 10^4$. $^{143}\text{Nd}/^{144}\text{Nd}_{\text{CHUR}} = 0.512630$, $^{176}\text{Hf}/^{177}\text{Hf}_{\text{CHUR}} = 0.282785$ [Bouvier et al., 2008] and $^{138}\text{Ce}/^{142}\text{Ce}_{\text{CHUR}} = 0.02256634$ [Willig and Stracke, 2019; normalized to AMES = 0.02257426].

Table 4: Chemical and isotopic compositions of the different reservoirs used in the modelling (Figures 5 and 6).

	R1 ⁽¹⁾	R2 ⁽²⁾	R3 ⁽³⁾	Oceanic crust ⁽⁴⁾	FOZO melt ⁽⁵⁾	FOZO source ⁽⁶⁾	kimberlite ⁽⁷⁾	lamproiite ⁽⁸⁾
La (ppm)	8.8	25.8	44.6	3.90	38.3	2.19	221.1	7.8
Ce (ppm)	2.4	9.6	71.3	12.00	79.8	5.03	419.8	298.1
Pr (ppm)			12.4	2.07	9.8	0.70	42.0	579.9
Nd (ppm)	6.8	19.3	51.0	11.18	42.6	3.47	161.1	64.3
Hf (ppm)					5.2	0.53	8.7	232.7
Ce/Ce*	0.15	0.20	0.74	1.03	1.01	0.99	1.06	1.02
¹³⁸ Ce/ ¹⁴² Ce	0.0228812	0.0227923	0.0226037	0.0225740	0.0225677	0.0225677		
¹⁴³ Nd/ ¹⁴⁴ Nd					0.512950	0.512950	0.511921	0.511929
¹⁷⁶ Hf/ ¹⁷⁷ Hf					0.283050	0.283050	0.282131	0.282418

⁽¹⁾R1= carbonate sediments from DSDP Site 495 (Pacific Ocean). REE contents are from *Patino et al.* [2000]. The initial Nd isotope composition is considered to be identical to that of Proterozoic seawater (data in *Derry and Jacobsen* [1988]). As there are no measurements for cerium isotopes, corresponding $\epsilon^{138}\text{Ce}$ values have been calculating assuming $\epsilon\text{Nd}/\epsilon\text{Ce} \sim -10$ (such a relationship agrees with calculations made in *Bellot et al.* [2015] and with the MORB-OIB relationship (mantle array) defined by *Willig and Stracke* [2019]). At 2.5 Ga reservoirs R1, R2 and R3 have a similar cerium isotope composition ($\epsilon^{138}\text{Ce}=-0.2$).

⁽²⁾R2 = Pacific Authigenic Weighted Mean sediments (PAWS, *Hole et al.* [1984]). The Ce isotope composition is considered to be identical to that of R1 2.5 Ga ago.

⁽³⁾R3 = mean composition of sedimentary material drilled in Kemadec, Tonga, Vanuatu, Marianas and Izu-Bonin trenches (data from *Plank* [2013]). The Ce isotope composition is considered to be identical to that of R1 2.5 Ga ago.

⁽⁴⁾Mean Oceanic Crust. REE contents are from *Hofmann* [1988]. The initial Nd isotope composition of OC is from *DePaolo* [1981]; the corresponding $\epsilon^{138}\text{Ce}$ values at 2.5 Ga have been calculating assuming $\epsilon\text{Nd}/\epsilon\text{Ce} \sim -10$ and is equal to -0.26.

⁽⁵⁾REE and Hf contents are the mean values of the 3 most primitive samples of Rurutu, Cook-Austral Islands (namely RRT-B21, RRT-B30 and RRT305-2 that are characterized by the highest MgO content: 10.6 - 12.6 wt%) amongst the samples listed in GEOROC [*Hauri and Hart*, 1993; 1997]. Nd and Hf isotope compositions are mean values measured on Rurutu young volcanics [*Stracke et al.*, 2005], the corresponding $\epsilon^{138}\text{Ce}$ value has been calculating assuming $\epsilon\text{Nd}/\epsilon\text{Ce} \sim -10$.

⁽⁶⁾The FOZO source concentrations are recalculated using 5% of batch melting and bulk partition coefficient of a garnet peridotite (55% olivine, 25% clinopyroxene, 11% orthopyroxene and 9% garnet). Dmineral-melt values are from *McKenzie and O'Nions* [1991].

⁽⁷⁾Swartuggens kimberlites, South Africa [*Coe et al.*, 2008; *Nowell et al.*, 2004; *Smith*, 1983; *Smith et al.*, 1985].

⁽⁸⁾Leucite Hills lamproites, Wyoming USA [*Mirnejad and Bell*, 2006; *Salter and Hart*, 1991].